

## MOLECULAR ENVIRONMENTS OF THREE LARGE SUPERNOVA REMNANTS IN THE THIRD GALACTIC QUADRANT: G205.5+0.5, G206.9+2.3, AND G213.0–0.6

YANG SU,<sup>1</sup> XIN ZHOU,<sup>1</sup> JI YANG,<sup>1</sup> XUEPENG CHEN,<sup>1</sup> YANG CHEN,<sup>2,3</sup> YI LIU,<sup>1</sup> HONGCHI WANG,<sup>1</sup>  
 CHONG LI,<sup>1,4</sup> AND SHAOBO ZHANG<sup>1</sup>

<sup>1</sup>*Purple Mountain Observatory and Key Laboratory of Radio Astronomy, Chinese Academy of Sciences, Nanjing 210008, China*

<sup>2</sup>*Department of Astronomy, Nanjing University, Nanjing 210023, China*

<sup>3</sup>*Key Laboratory of Modern Astronomy and Astrophysics, Nanjing University, Ministry of Education, Nanjing 210023, China*

<sup>4</sup>*University of Chinese Academy of Sciences, 19A Yuquan Road, Shijingshan District, Beijing 100049, China*

### ABSTRACT

We present CO observations toward three large supernova remnants (SNRs) in the third Galactic quadrant using the Purple Mountain Observatory Delingha 13.7 m millimeter-wavelength telescope. The observations are part of the high-resolution CO survey of the Galactic plane between Galactic longitudes  $l = -10^\circ$  to  $250^\circ$  and latitudes  $b = -5^\circ$  to  $5^\circ$ . CO emission was detected toward the three SNRs: G205.5+0.5 (Monoceros Nebula), G206.9+2.3 (PKS 0646+06), and G213.0–0.6. Both of SNRs G205.5+0.5 and G213.0–0.6 exhibit the morphological agreement (or spatial correspondences) between the remnant and the surrounding molecular clouds (MCs), as well as kinematic signatures of shock perturbation in the molecular gas. We confirm that the two SNRs are physically associated with their ambient MCs and the shock of SNRs is interacting with the dense, clumpy molecular gas. SNR G206.9+2.3, which is close to the northeastern edge of the Monoceros Nebula, displays the spatial coincidence with molecular partial shell structures at  $V_{\text{LSR}} \sim 15 \text{ km s}^{-1}$ . While no significant line broadening has been detected within or near the remnant, the strong morphological correspondence between the SNR and the molecular cavity implies that SNR G206.9+2.3 is probably associated with the CO gas and is evolving in the low-density environment. The physical features of individual SNRs, together with the relationship between SNRs and their nearby objects, are also discussed.

*Keywords:* ISM: individual (G205.5+0.5, G206.9+2.3, and G213.0–0.6) – ISM: molecules – supernova remnants

## 1. INTRODUCTION

Most core-collapse supernovae (SNe) from high-mass stars may explode promptly and are thought to be associated with the molecular clouds (MCs) from which they were born. Therefore, the subsequent supernova remnants (SNRs) may evolve close to their parental MCs or the nearby molecular environment. So far, there are several signposts to show the physical contact/interaction between SNRs and their molecular environments, e.g., the presence of 1720 MHz OH maser emission, molecular line broadenings or asymmetric profiles, high molecular line ratios between different excitation states, detection of H<sub>2</sub> and/or [Fe II] lines in near-infrared, specific infrared colors within an SNR, and often used morphological correspondence in multiwavelength with SNR features (see Jiang et al. 2010). It is also important to study the interplay of SNR–MC systems for investigating various physical and astrophysical processes therein (e.g., Chen et al. 2014; Dubner & Giacani 2015; Slane et al. 2015).

There are currently 294 SNRs known in the Milky Way (Green 2014) and about 70 of them are confirmed or suggested to be associated with MCs (refer to, e.g., Jiang et al. 2010; Chen et al. 2014). CO, as an indicator of H<sub>2</sub>, is the most widely used tracer of MCs and it is very common and useful when investigating the nature of the molecular ISM in galaxies. CO observations also play a key role in studying the molecular environment and physical characteristics of SNR–MC interacting systems. To date, three large-scale, systematic CO surveys were performed to investigate the SNR–MC association (Huang & Thaddeus 1986; Jeong et al. 2012; Kilpatrick et al. 2016). Recently, several individual SNR–MC systems were also investigated using CO lines (e.g., SNR W44 by Anderl et al. 2014; SNR Cassiopeia A by Kilpatrick et al. 2014; SNR IC 443 by Su et al. 2014a; SNR G22.7–0.2 by Su et al.

2014b; SNR G127.1+0.5 by Zhou et al. 2014; SNR G18.8+0.3 by Paron et al. 2015; SNR G357.7+0.3 by Rho et al. 2017; SNR RCW 86 by Sano et al. 2016; SNR Tycho by Zhou et al. 2016a and Chen et al. 2016; and SNR HB 3 by Zhou et al. 2016b). Nevertheless, few studies have been conducted to investigate the SNRs’ molecular environment in the third Galactic quadrant.

The Milky Way Imaging Scroll Painting (MWISP) project<sup>1</sup> is a large <sup>12</sup>CO ( $J=1-0$ ), <sup>13</sup>CO ( $J=1-0$ ), and C<sup>18</sup>O ( $J=1-0$ ) survey of the northern Galactic plane. The systematic and unbiased CO survey, which has high spatial ( $\sim 50''$ ) and velocity ( $\sim 0.2 \text{ km s}^{-1}$ ) resolution, will provide the detailed distributions and fully sampled images of molecular gas from  $l = -10^\circ$  to  $250^\circ$  and latitudes from  $b = -5^\circ$  to  $5^\circ$ . The high-quality CO data also provide us with a good opportunity to study the molecular environment of extended SNRs from large scale to small scale. Especially for SNRs with large angular size, the unbiased CO survey can offer detailed molecular gas information on SNR–MC interactions.

In this paper, we aim to investigate the molecular environment of three large SNRs: G205.5+0.5 (Monoceros Nebula), G206.9+2.3 (PKS 0646+06), and G213.0–0.6 from our new CO survey. The three SNRs are all in the third Galactic quadrant and their angular sizes are  $\gtrsim 1^\circ$ . Benefiting from the large-scale spectroscopic mapping of the CO survey, we analyzed the correlation between these three remnants and their molecular environment mainly from SNR–MC’s morphological correspondences (e.g., molecular arc, shell, cavity, interface, and coincidence in multiwavelength emission, etc.), molecular line diagnostics (e.g., broad molecular line features or asymmetric line profiles), and special kinematic fea-

<sup>1</sup> <http://www.radioast.nsdc.cn/mwisp.php>

tures (e.g., velocity gradient revealed in the position–velocity (PV) diagram).

In Section 2, we describe the CO observation and the data reduction, and in Section 3 we present our results and discussions for individual SNRs. Finally, a summary is given in Section 4.

## 2. CO DATA FROM MWISP

The MWISP project, which started in 2011, is a large CO survey using the 13.7 m millimeter-wavelength telescope located at Delingha in China. The  $^{12}\text{CO}$  ( $J=1-0$ ),  $^{13}\text{CO}$  ( $J=1-0$ ), and  $\text{C}^{18}\text{O}$  ( $J=1-0$ ) observations are performed simultaneously with the nine-beam Superconducting Spectroscopic Array Receiver (SSAR) system (Shan et al. 2012). A Fast Fourier Transform Spectrometer (FFTS) with a total bandwidth of 1 GHz provides 16,384 channels, resulting in a spectral resolution of 61 kHz, equivalent to a velocity resolution of  $\sim 0.17 \text{ km s}^{-1}$  at 110 GHz. The intermediate frequency (IF) band is  $2.64 \pm 0.5$  GHz so that three CO isotope lines ( $^{12}\text{CO}$  line at 115.271 GHz,  $^{13}\text{CO}$  line at 110.201 GHz, and  $\text{C}^{18}\text{O}$  line at 109.782 GHz) can be covered by the 1 GHz band when the local oscillator (LO) is at 112.6 GHz. We should specify that the FFTS is sideband separated and  $^{12}\text{CO}$  line is in the upper while  $^{13}\text{CO}$  and  $\text{C}^{18}\text{O}$  are in the lower band. The half-power beamwidth (HPBW) of the telescope is about  $50''$  and the pointing accuracy is better than  $5''$  in all observing epochs. The main beam efficiency and other useful parameters can be found from the status report<sup>2</sup>.

All covered sky will be divided into 10,941 cells and each cell with a dimension of  $30' \times 30'$  is scanned along the Galactic longitude and the Galactic latitude to reduce the fluctuation of noise. Observations are conducted in position-switch On-The-Fly (OTF) mode, scanning each

cell at a rate of  $50''$  (or  $75''$ ) per second with a dump time of 0.3 s (or 0.2 s). Before the observation, the background reference region ( $8' \times 8'$ ) near the cell has been carefully checked ( $\lesssim 0.3$  K in  $^{12}\text{CO}$  emission at any points) to ensure no or little emission from the off region. In addition, the water vapor in the terrestrial atmosphere contributes noise in our CO spectra. Our survey requires relatively dry and stable atmosphere conditions to guarantee the quality of the data. As a result, typical system temperatures are within  $\sim 190$ –350 K at the upper sideband and  $\sim 140$ –230 K at the lower sideband depending on weather conditions, cell's elevations, and off positions.

All data were reduced using the GILDAS/CLASS package<sup>3</sup>. After the first order (linear) baseline fitting and mosaicing the image, the final three-dimensional (3D) cube data were obtained with a grid spacing of  $30''$ . The typical sensitivity (RMS) is about 0.5 K for  $^{12}\text{CO}$  ( $J=1-0$ ) at the channel width of  $0.16 \text{ km s}^{-1}$  and 0.3 K for  $^{13}\text{CO}$  ( $J=1-0$ ) and  $\text{C}^{18}\text{O}$  ( $J=1-0$ ) at  $0.17 \text{ km s}^{-1}$ . As of this writing the MWISP project has completed about half of its planned area of coverage and the three large SNRs G205.5+0.5, G206.9+2.3, and G213.0–0.6, including their nearby regions, were all mapped from 2012 January to 2016 April. Generally,  $\text{C}^{18}\text{O}$  ( $J=1-0$ ) emission is too weak to give any further details toward these SNRs. Our discussions will focus primarily on  $^{12}\text{CO}$  and  $^{13}\text{CO}$  data.

## 3. RESULTS AND DISCUSSIONS

### 3.1. SNR G205.5+0.5 (*Monoceros Nebula*)

G205.5+0.5 (*Monoceros Nebula*) is a very large SNR with a size of  $\sim 220'$ . Xiao & Zhu (2012) showed that the radio spectral index ( $\alpha$ ) of the remnant is about  $-0.41$ , derived from 21 cm, 11 cm, and 6 cm radio continuum data, which is generally consistent with

<sup>2</sup> <http://www.radioast.nsdc.cn/mwisp.php>

<sup>3</sup> <http://www.iram.fr/IRAMFR/GILDAS>

the result of previous works (Dickel & Denoyer 1975; Graham et al. 1982). Throughout this paper, all directions are described in Galactic coordinates to match the MWISP CO survey. The bright Rosette Nebula (Sh 2-275) and open cluster NGC 2264 (Sh 2-273) are located near the southern and northwestern boundary of the remnant, respectively. Odegard (1986) suggested that the SNR is probably located behind the Rosette Nebula because of the absorption of the remnant's nonthermal emission by the southern H II region Sh 2-275. Xiao & Zhu (2012) also suggested that the SNR is probably associated with the Rosette Nebula because of the identified western partial shell structures at  $\sim 15 \text{ km s}^{-1}$  using the new Arecibo HI 21 cm data. The remnant displays contrasting optical filamentary structures mainly on its northwestern, western, and southwestern edges. These sharp optical filaments, especially toward the western boundary of the remnant, are well correlated with the bright radio shells (Davies et al. 1978) and the X-ray emission regions (Leahy et al. 1985, 1986). According to the Sino-German 6 cm survey, Gao et al. (2011) found that the magnetic field is mainly aligned with the western shell of the remnant.

In our large CO survey with spatial resolution better than  $\sim 1'$ , we detected molecular gas over a wide velocity range from  $-10$  to  $50 \text{ km s}^{-1}$  toward SNR G205.5+0.5 (Figure 1). Obviously, two large giant molecular cloud (GMC) complexes are associated with the southern Rosette Nebula (MCs in the lower-left corner of Figure 1,  $V_{\text{LSR}} \sim 3\text{--}18 \text{ km s}^{-1}$ ) and the northwestern NGC 2264 (MCs in the upper-right corner of Figure 1,  $V_{\text{LSR}} \sim 3\text{--}12 \text{ km s}^{-1}$ ), respectively. Our unbiased CO survey revealed huge amounts of molecular gas in the velocity range from 25 to  $50 \text{ km s}^{-1}$ . The  $25\text{--}50 \text{ km s}^{-1}$  MCs, which have small sizes and weak CO emission, are distributed widely and separately over the field of view (FOV). The CO emis-

sion of the  $25\text{--}50 \text{ km s}^{-1}$  components along the line of sight (LOS) is probably from the distant molecular gas (e.g., the Perseus and/or the Outer arm in the direction). We did not find any evidence of physical connection between the  $V_{\text{LSR}} \gtrsim 25 \text{ km s}^{-1}$  molecular gas and the remnant. We will not discuss the MC components and we will mainly focus on the  $V_{\text{LSR}} \lesssim 25 \text{ km s}^{-1}$  MCs in this section.

When the SNR's shock is encountering a dense medium, the shock will compress, heat, accelerate, and even dissociate molecules, which will lead to a wide variety of observable effects. The material may carry enough momentum to accelerate the molecular gas to broad velocity width. Generally, the asymmetric line profiles from  $^{12}\text{CO}$  emission usually imply the turbulent molecular gas because such emission is more easily influenced by the shock. On the contrary,  $^{13}\text{CO}$  emission is optically thin, which is not heavily influenced by SNR's shock. In another words,  $^{12}\text{CO}$  emission is from the enveloping layer of low-density gas and is readily perturbed by local turbulence while  $^{13}\text{CO}$  emission is not so. The line peak of  $^{13}\text{CO}$  emission is thus a good indicator of the LSR velocity of unperturbed clouds. As a result, the asymmetric line profiles of  $^{12}\text{CO}$  can be picked out from the LSR velocity range of the  $^{13}\text{CO}$  component (e.g., refer to the blue broadening from Figures 7 and 8 for shocked gas a; the red broadening from Figures 3 and 8 for shocked gas d–e).

Actually, several signatures of SNR–MC interaction toward the remnant are revealed in our CO observations. First, the molecular gas at  $V_{\text{LSR}} \sim 19 \text{ km s}^{-1}$  (in the interval of  $18\text{--}23 \text{ km s}^{-1}$ ) seems to be concentrated in the center region of SNR G205.5+0.5 (Figure 2) and this molecular gas exhibits weak redshifted broadening in  $^{12}\text{CO}$  emission (e.g., the typical spectra of d and e in Figure 8). The broadening of the two positions is not very large ( $\sim 2\text{--}3 \text{ km s}^{-1}$  from the  $^{13}\text{CO}$  peak) but can be easily

discerned from the asymmetric  $^{12}\text{CO}$  profile. It is worth noting that the weak emission in  $^{12}\text{CO}$  is systematic redshifted with respect to the unperturbed clouds traced by  $^{13}\text{CO}$  (Figure 3), which indicates the  $^{12}\text{CO}$  wing component in the velocity interval of  $\sim 19\text{--}22\text{ km s}^{-1}$  and the  $^{13}\text{CO}$  component at a slightly low LSR velocity of  $\sim 19\text{ km s}^{-1}$  are apparently connected. Therefore, the weak emission seen in the redshifted  $^{12}\text{CO}$  wing (d-f in Figure 8) and the  $^{13}\text{CO}$  emission is from the coherent molecular gas, but not from the separated source with slightly different distances along the LOS. Generally, the redshifted broadening of d-f is not very large. High J CO lines (e.g., 2-1 and/or 3-2) may be useful for investigating these regions in the future.

Second, two partial shell structures traced by  $^{12}\text{CO}$  in  $V_{\text{LSR}}=3\text{--}6\text{ km s}^{-1}$  and  $V_{\text{LSR}}=27\text{--}29.5\text{ km s}^{-1}$  seem to be correlated with the southwestern (Figure 4) and the southeastern (Figure 5) radio emission, respectively. Especially, the partial shell structure revealed by the  $3\text{--}6\text{ km s}^{-1}$  molecular component is as long as  $52'$ , or  $\sim 24$  pc at a distance of 1.6 kpc (see below). We suggest that the molecular structures are probably related to the remnant; nevertheless, the CO emission of the two shells is too weak to be studied in detail.

Third, in the western edge of the SNR, an interesting MC structure is found to be physically associated with the remnant (see the right rectangle in Figure 1). Figure 6 displays striking spatial coincidence between the  $V_{\text{LSR}}\sim 5\text{ km s}^{-1}$  MC structure (in the interval of  $3\text{--}12\text{ km s}^{-1}$ ) and the remnant's shell in the west boundary of the SNR. In the left panel of this figure, a bright optical filament, as well as the radio ridge seen in 21 cm data, is elongated along the northeast-southwest direction. Note that both of the 11 cm (the Effelsberg 11 cm survey, see Furst et al. 1990) and the 6 cm (the Parkes-MIT-NRAO (PMN) 4850 MHz survey, see Condon et al.

1993) radio emission also can be discerned from the ambient background emission in such a region with higher resolution and sensitivity. The southeastern boundary of the MC is very sharp and follows exactly the remnant's shell and resembles the outline of the bright optical filaments and the radio ridge. That is, the molecular gas forms a wall facing the bright optical filaments or the SNR's shell. We found line-broadening features in such molecular gas (e.g., see a-c in Figure 8). Especially, a narrow component centered at  $5\text{ km s}^{-1}$  in the  $^{13}\text{CO}$  line, together with a blue wing component down to  $-2\text{ km s}^{-1}$  in  $^{12}\text{CO}$  line, is clearly recognized at position c, which can also be confirmed from Figure 7. It seems that the shocked gas traced by the line broadening is near the region of the  $^{12}\text{CO}$  intensity maximum (see the red contours in the left panel of Figure 6). Furthermore, a substantial velocity gradient of the molecular gas (Figure 7), is found to be mostly orthogonal to the shell of the SNR (refer to the direction denoted by the arrow in Figure 6). The velocity gradient of  $\sim 0.9\text{ km s}^{-1}\text{arcmin}^{-1}$  (or  $\sim 1.9\text{ km s}^{-1}\text{pc}^{-1}$  at 1.6 kpc) is very likely related to the SNR's shock.

We thus suggest that the MCs at  $\sim 5\text{ km s}^{-1}$  and  $\sim 19\text{ km s}^{-1}$  are both associated with the remnant. Figure 9 shows the gas distribution of the two components. The  $5\text{ km s}^{-1}$  molecular gas (blue) lies in front of the remnant and has been accelerated toward us, which can be confirmed from the high optical obscuration (the left panel of Figure 6) and the molecular gas's blueshifted profile in the direction (e.g., position c in Figure 8). The  $19\text{ km s}^{-1}$  gas (red), however, is probably on the farside of the remnant because of their little evidence of associated LOS obscuration and the redshifted profiles (see asymmetric line-broadening features at positions d-f in Figure 8). It is worth mentioning that not all molecular gas in Figure 9 is interacting with SNR G205.5+0.5. For ex-

ample, the blue part in the upper-right corner of Figure 9, which belongs to the NGC 2264 GMC complex and is located at a distance of  $\sim 740\text{--}900$  pc (e.g., Sung et al. 1997; Baxter et al. 2009; Kamezaki et al. 2014) is probably not related to the SNR.

The excellent spatial correlation between the ionized gas traced by optical data and the molecular gas traced by CO data, as well as broad wings of line profiles in some regions, suggests that SNR G205.5+0.5 is interacting with the ambient molecular gas. We note that the nearby Rosette Nebula is also interacting with the same CO component, which is consistent with the result of other studies (e.g., Schneider et al. 1998; Dent et al. 2009). In Figure 9, the Rosette Nebula is found to be surrounded by the  $3\text{--}12\text{ km s}^{-1}$  and  $18\text{--}23\text{ km s}^{-1}$  MCs, indicating a connection between them. A detailed study between the Rosette Nebula and its ambient MCs will be presented in a forthcoming paper (C. Li et al. 2017, in preparation).

Furthermore, based on the 3D extinction map from Green et al. (2015), we can estimate the distance toward the molecular gas associated with SNR G205.5+0.5 to constrain the distance of the SNR. We select a region centered at ( $l = 204^\circ.107$ ,  $b = 0^\circ.471$ ), which is just located at the CO emission peak of the  $5\text{ km s}^{-1}$  MCs (see the maximum of red contours in the left panel of Figure 6). We find a rapid increase for this region at a distance modulus (DM) of  $\sim 11$  ( $\sim 1.6$  kpc). On the other hand, several regions are selected for the  $19\text{ km s}^{-1}$  MCs, which are at  $\text{DM} \sim 11\text{--}11.5$  ( $\sim 1.6\text{--}2$  kpc). Since the  $5\text{ km s}^{-1}$  and  $19\text{ km s}^{-1}$  MCs are both physically associated with the SNR, it indicates that SNR G205.5+0.5 is very likely located at a distance of  $\sim 1.6$  kpc. This value is coincident within the errors with a distance of 1.6 kpc according to the association between the SNR and the Rosette Nebula (refer to works of distance esti-

mate of the Nebula; e.g., Hensberge et al. 2000; Park & Sung 2002).

In combination with the above analysis, we suggest that SNR G205.5+0.5 and the nearby Rosette Nebula are associated and both of the two extended sources are at a similar distance of 1.6 kpc. Our new CO analysis confirms the speculation that SNR G205.5+0.5 is probably associated with the nearby Rosette Nebula (e.g., Oliver et al. 1996). Using the CfA 1.2 m millimeter-wavelength telescope, Oliver et al. (1996) found that MCs 18-24 (see Tables 1 and 2, Figures 2 and 6 in their paper) lie toward the two extended sources and are probably related to their nearby bright optical and radio emission. They estimated the emission-weighted average kinematic distance of 1.6 kpc for these MCs, which is in agreement with the photometric distance to the Rosette Nebula. Recently, Xiao & Zhu (2012) revealed partial neutral hydrogen shell structures outside the western boundary of the remnant. The interesting HI shell in the velocity interval of  $5\text{--}25\text{ km s}^{-1}$  seems to relate to SNR G205.5+0.5 and the Rosette Nebula, which strengthens the association between them.

Using the relation of initial total energy  $E$  and the ambient gas density  $n_0$  (e.g.,  $E_{51} = 5.3 \times 10^{-8} n_0^{1.12} (\text{cm}^{-3}) v_{\text{sh}}^{1.40} (\text{km s}^{-1}) R^{3.12} (\text{pc})$  erg, Equation 26 in Chevalier 1974), the ambient density of the remnant is  $\sim 0.4 E_{51}^{0.893} \text{ cm}^{-3}$  for a remnant's radius of  $\sim 51$  pc (e.g., size of  $\sim 220'$  at a distance of 1.6 kpc) and an expansion velocity of  $\sim 50\text{ km s}^{-1}$  (Wallerstein & Jacobsen 1976; Welsh et al. 2001; Dirks & Meyer 2016), where  $E_{51}$  is the initial total energy of the remnant in units of  $10^{51}$  ergs. The low shock velocity of  $\sim 50\text{ km s}^{-1}$  is consistent with the result that the remnant has weak [O III] emission (Fesen et al. 1985). If the remnant is expanding into the ambient gas with such velocity, its age is estimated to be  $\sim 3.0 \times 10^5$  years based

on the radiative-phase solution (e.g.,  $R \sim t^{0.305}$ , Equation 25 in Chevalier 1974).

An extended or confused source, 3EG J0634+0521 (Hartman et al. 1999; Casandjian & Grenier 2008), and a TeV source, HESS J0632+057 (Aharonian et al. 2007), seem to be located close to the interface between SNR G205.5+0.5 and the Rosette Nebula (see blue circles in Figure 1). However, there is no further evidence to show the association between the two high-energy sources and the SNR. On the other hand, 2FGL sources of J0636.0+0554 and J0637.8+0737 (Nolan et al. 2012) are located close to the molecular gas revealed by our new CO survey (two little circles in Figure 9). Very recently, extended gamma-ray emission from *FERMI*/LAT observations was found inside the remnant (see Figures 3 and 4 in Katagiri et al. 2016). According to our study, the MC concentration in the velocity intervals of  $3\text{--}12\text{ km s}^{-1}$  and  $18\text{--}23\text{ km s}^{-1}$ , which is shown to be associated with the remnant, is consistent well with the distribution of the background-subtracted gamma-ray emission. The confirmation of SNR-MC interaction toward SNR G205.5+0.5, as well as the spatial coincidences between the shocked molecular gas and the gamma-ray emission, indicates that the extended gamma-ray emission inside the remnant is very likely from the hadronic scenario. In the scenario, the high-energy emission near the old SNR can be naturally explained by the decay of neutral pions produced in interactions between hadrons accelerated by the remnant's shock and its ambient dense molecular gas, which is also consistent with the theoretical analysis (e.g., Yamazaki et al. 2006; Fujita et al. 2009).

### 3.2. SNR G206.9+2.3 (PKS 0646+06)

SNR G206.9+2.3, which is also known as PKS 0646+06, is a faint and extended nonthermal radio source near the Monoceros Nebula (Figures 1 and 10). The radio spectral index of the SNR is about  $-0.45$  (Graham et al. 1982), which

was recently confirmed by Gao et al. (2011, i.e.,  $\alpha = -0.47$ ). The remnant, which has relatively strong radio emission in its northwest region, roughly shows an elliptical shape in radio emission (see contours in Figure 10). Near the northwestern radio peak, the optical data reveals a bright thin filament with a relatively high density (e.g.,  $n_e \sim 800\text{ cm}^{-3}$ , position 1 at  $l = 206^\circ 77$  and  $b = 2^\circ 61$  in Fesen et al. 1985). The enhanced X-ray emission from Einstein observations, which is close to the northwestern radio peak of the remnant, is suggested to be associated with SNR G206.9+2.3 (Leahy 1986). Both of the X-ray and optical studies indicate that the SNR is probably evolving in low-density environment (Leahy 1986; Ambrocio-Cruz et al. 2014) except for the relatively high density region near the radio peak (e.g., position 1 mentioned above).

We covered a large CO map toward SNR G206.9+2.3 and the nearby regions with high sensitivity and resolution. CO emission is very weak in the direction of the remnant except for the nearby MC complex at  $V_{\text{LSR}} \sim 15\text{ km s}^{-1}$  (in the velocity interval of  $11\text{--}19\text{ km s}^{-1}$ , see Figure 10). The main body of the MC complex, which has weak  $^{13}\text{CO}$  emission over the FOV (see green parts in the figure), displays curved partial shell structures and extends over 5 degrees in longitude from  $204^\circ 9$  to  $210^\circ 3$ . We find that the MC complex has a complicated velocity structure (Figure 11). The  $13\text{--}15\text{ km s}^{-1}$  molecular gas, together with the outside large-scale partial shell structures at  $15\text{--}17\text{ km s}^{-1}$ , seems to form a molecular void toward the SNR. The curvature of the partial shell structures points in the direction from the SNR to the outside shell-like MCs. It is interesting to note that SNR G206.9+2.3 roughly lies in the geometrical center of the MC's void, which agrees well with the low extinction values in the direction (see the case of G206.9+2.3 in Table 2 of Fesen et al. 1985). Some patches of molecular gas at an

LSR velocity of  $\sim 13 \text{ km s}^{-1}$  are found to coincide with the northwestern radio peak of the remnant (e.g.,  $l \sim 206^\circ.85$  and  $b \sim 2^\circ.55$ , near the red box shown in Figure 11), which is consistent with the fact of the relatively high density there based on optical observation (refer to position 1 of SNR G206.9+2.3 in [Fesen et al. 1985](#)).

In particular, the  $13\text{--}15 \text{ km s}^{-1}$  molecular gas is well along the southeastern boundary of the SNR. The close-up partial shell structure in the velocity interval of  $14\text{--}15 \text{ km s}^{-1}$  is presented in Figure 12, in which the SNR is clearly surrounded by molecular shell from the east to the south. Moreover, a velocity gradient of  $\sim 0.3 \text{ km s}^{-1} \text{ arcmin}^{-1}$  (or  $\sim 0.6 \text{ km s}^{-1} \text{ pc}^{-1}$  at 1.6 kpc, see the PV diagram in Figure 13) is detected to be perpendicular to (see the arrow in Figure 12) the shell structure, which probably indicates that the molecular gas is expanding outward at several kilometers per second.

If SNR G206.9+2.3 is associated with the  $\sim 15 \text{ km s}^{-1}$  molecular gas cavity, the kinematic distance of the remnant is estimated to be  $\sim 1.6$  kpc based on the A5 rotation curve model of [Reid et al. \(2014\)](#). The remnant's angular size of  $\sim 60'$  thus corresponds to a physical radius of  $\sim 14.0$  pc. Using the relation of the blast-wave energy  $E$  and the cloud parameters  $n_c$  and  $v_c$  (e.g.,  $E_{51} = 2 \times 10^{-9} \beta^{-1} n_0 (\text{cm}^{-3}) v_{\text{sh}}^2 (\text{km s}^{-1}) R^3 (\text{pc})$  erg, Equation 26 in [McKee & Cowie 1975](#)), we can roughly estimate the shock velocity of the remnant. Adopting the numerical factor  $\beta=1$ , explosion energy  $E=10^{51}$  ergs, and the density  $n_0 \sim 0.1 \text{ cm}^{-3}$  (the upper limit, see discussions in [Leahy 1986](#)), the shock velocity of the remnant is greater than  $\sim 1000 \text{ km s}^{-1}$ . Therefore, SNR G206.9+2.3 is probably in the Sedov-Taylor phase and the age of the remnant is estimated to be less than 4000 years.

Finally, it should be noted that, although the above morphological correspondences may indicate an association between the SNR and the

$15 \text{ km s}^{-1}$  molecular gas, there are few kinematic signatures to suggest an interaction scenario directly (e.g., no significant line broadening is detected within or near the remnant). It probably indicates that the SNR is evolving in the molecular cavity, which is in agreement with the low density there and the surrounding molecular shell structures. Further observations and analysis of the remnant are required to draw any firm conclusions.

### 3.3. SNR G213.0-0.6

Using the 863 MHz data and the 2.695 GHz data from the Effelsberg survey, [Reich et al. \(2003\)](#) firstly identified G213.0-0.6 as an old SNR with  $\alpha \sim -0.4$ . The remnant displays partial shell-like structures on a large scale and it has low radio surface brightness. On the other hand, a large complex of HII region Sh 2-284, which has bright optical, infrared, and radio emission, is located to the southwestern boundary of the remnant. The remnant was also named as G213.3-0.4 according to the new optical H $\alpha$  imaging and relatively high-resolution radio observations from the PMN survey at 4.85 GHz and NRAO/VLA Sky Survey (NVSS) at 1.4 GHz ([Stupar & Parker 2012](#)). Following Green's SNR catalog ([Green 2014](#)), we use SNR G213.0-0.6 as its name throughout this paper. Generally speaking, the SNR is less studied because of its large angular size and low radio surface brightness.

Figure 14 shows the distribution of the molecular gas toward SNR G213.0-0.6. Given the very fragmented structures of the SNR in radio emission, optical contours from the Southern H $\alpha$  Sky Survey ([Parker et al. 2005](#)) have been made to trace the SNR and the southwestern HII region Sh 2-284. In the direction of SNR G213.0-0.6, molecular gas is mainly concentrated in the velocity range of  $0\text{--}60 \text{ km s}^{-1}$ . CO emission is very weak toward SNR G213.0-0.6, while the emission outside the remnant is relatively strong. This fact probably corresponds

to the faint radio emission on a large scale because the density of the SNR's environment is relatively low. In Figure 14, the southwestern molecular gas is obviously related to H II region Sh 2-284. The relationship between the SNR and its southwestern extended source Sh 2-284 is also investigated.

We find that molecular gas at systemic velocity of  $8\text{--}11\text{ km s}^{-1}$  seems to be located around the boundary of SNR G213.0-0.6, especially to the southeast and northwest (Figure 15). In projection, the H $\alpha$  and radio emission is enhanced toward the southeastern boundary of the remnant (see the box region in Figure 15) coincident with an MC with a velocity interval of  $6.5\text{--}12\text{ km s}^{-1}$ . The MC, which is found to be along the boundary of the remnant from the northeast to the southwest, displays a prominent velocity gradient ( $\sim 0.7\text{ km s}^{-1}\text{arcmin}^{-1}$ , or  $\sim 2.4\text{ km s}^{-1}\text{pc}^{-1}$  at 1.0 kpc, see below) perpendicular to the main axis of the  $^{12}\text{CO}$  emission (see the arrow in Figure 16). The PV diagram of the molecular gas (Figure 17) reveals the detailed velocity structure along the MC, as well as an interesting arc structure seen in the map. We suggest that this feature is probably related to the remnant's shock. Stupar & Parker (2012) found that the density in the region of the H $\alpha$  peak is relatively high based on optical observations ( $n_e \sim 10^2\text{ cm}^{-3}$ , refer to Table 2 in their paper). This result suggests that SNR G213.0-0.6 is interacting with a clumpy interstellar medium, which agrees with the CO emission near the H $\alpha$  peak using our CO data (Figure 16). Assuming a constant value of  $X_{\text{CO}} = 2 \times 10^{20}\text{ cm}^{-2}\text{K}^{-1}\text{km}^{-1}\text{s}$  (Bolatto et al. 2013), the MC's thickness of  $4'$ , and a distance of 1 kpc (see below), the density of the MC is about  $300d_{1\text{kpc}}^{-1}\text{ cm}^{-3}$ , which is consistent with the result of the optical study (Stupar & Parker 2012). The interesting MC, as well as its velocity structure, suggests that the molecular gas

with LSR velocity  $\sim 8\text{--}11\text{ km s}^{-1}$  is probably interacting with SNR G213.0-0.6.

CO emission of this molecular component is also concentrated in the northwest of the remnant, in which the H $\alpha$  and radio emission displays blow-out structure (see the northwestern region in Figure 15). An MC with line broadening (several  $\text{km s}^{-1}$ , see the right panel of Figure 18) is revealed in the region (see the relatively large red circle in the northwest of Figure 15). The H $\alpha$  emission, together with the PMN 4850 MHz radio emission, appears to be locally enhanced in such a region.

In combination with the morphological correspondence and the broadening of CO profiles, we suggest that molecular gas at  $V_{\text{LSR}} \sim 9\text{ km s}^{-1}$  is physically associated with the remnant. Accordingly, the kinematic distance of the remnant is about 0.7-1.0 kpc (e.g.,  $V_{\text{LSR}} \sim 8\text{--}11\text{ km s}^{-1}$  from Figure 17) based on the A5 rotation curve model of Reid et al. (2014). The estimated kinematic distance of the remnant is consistent well with that of the empirical radio surface-brightness-to-diameter ( $\Sigma-D$ ) relation. Using the updated  $\Sigma-D$  relation for SNRs and the probability-density-function-based method (Pavlovic et al. 2014), the distance of the SNR is estimated to be  $1.0 \pm 0.18$  kpc. We also estimate that the  $8\text{--}11\text{ km s}^{-1}$  molecular gas (e.g., at position ( $l = 213^\circ 798$ ,  $b = -0^\circ 949$ ), see Figure 16) is at  $\text{DM} \sim 10$  (or  $\sim 1.0$  kpc) according to the 3D extinction map (Green et al. 2015). The estimated distance is in good agreement with the result from the above  $\Sigma-D$  and kinematic methods. We thus adopt 1 kpc as the distance to SNR G213.0-0.6.

The angular size ( $\sim 3^\circ 4 \times 2^\circ 3$ , accounting for the blow-out structure in the northwestern region) of the remnant corresponds to a physical size of  $59\text{ pc} \times 40\text{ pc}$  at about 1 kpc distance. The large physical size, the low radio surface brightness, and the relatively high density near the boundary of the rem-

nant indicates that SNR G213.0–0.6 probably exploded in a low-density cavity and now is interacting with the surrounding clumpy interstellar medium. Assuming the mean density of  $n_0 \sim 0.1 \text{ cm}^{-3} \equiv n_{-1}$  and the SNR's explosion energy of  $E \sim 10^{51} \text{ erg} \equiv E_{51}$ , the remnant's equivalent radius of 24.3 pc yields a shock velocity of about  $590(E_{51}/n_{-1})^{0.5} \text{ km s}^{-1}$ . The age of the remnant in the radiative phase is thus about  $1.1(n_{-1}/E_{51})^{0.5} \times 10^4$  years.

On the other hand, MCs at  $V_{\text{LSR}}=42\text{--}48 \text{ km s}^{-1}$  (in the velocity interval of  $35\text{--}54 \text{ km s}^{-1}$ , see Figure 19) are probably from the Milky Way's Perseus arm and/or the Norma (Outer) arm at a kinematic distance of  $\sim 4.5\text{--}5.5$  kpc (e.g., refer to the rotation model of Reid et al. 2014). These MCs are clearly associated with H II region Sh 2-284 and a group of early-type OB stars (see the region of Sh 2-284 in this figure). We also find that molecular gas at  $V_{\text{LSR}}=28 \text{ km s}^{-1}$  (in the velocity interval of  $24\text{--}33 \text{ km s}^{-1}$ , see Figure 20) seems to be located between the southwestern boundary of SNR G213.0–0.6 and H II region Sh 2-284. The  $28 \text{ km s}^{-1}$  MC component is probably also related to the H II region Sh 2-284 because the blueshifted CO gas with respect to the  $42\text{--}48 \text{ km s}^{-1}$  molecular component has corresponding dark patches against the bright optical emission. The molecular gas presents blueshifted wing profiles on the side of the cloud facing H II region Sh 2-284 (e.g., see the red box and its spectra in Figure 20). Accounting for the low metallicity in the H II region, the distance of Sh 2-284 is estimated to be about 4 kpc (Delgado et al. 2010; Cusano et al. 2011) or 4.5 kpc (Negueruela et al. 2015), which is in good agreement with the kinematic distance from our CO observations (e.g., the MCs with  $V_{\text{LSR}} \sim 42\text{--}48 \text{ km s}^{-1}$  physically associated with the H II region Sh 2-284). However, we do not find any convincing evidence of SNR–MC interaction for such molecular components.

Finally, many MCs outside the SNR can be seen in the north of Figure 19, in which several early-type OB stars seem to be related to these MCs. For example, B0 star HD 289291 ( $211^\circ.768, +0^\circ.747$ , the upper-right cross in Figure 19) is very likely responsible for its northern MC shell at  $V_{\text{LSR}} \sim 45 \text{ km s}^{-1}$  (see the upper-right corner in Figure 19). It is interesting to note that a maser source G211.59+01.05 at  $V_{\text{LSR}} \sim 45 \pm 5 \text{ km s}^{-1}$  (see red triangle in Figure 19) is exactly located in the MC shell. The parallax distance of the maser is about 4.4 kpc ( $0.228 \pm 0.007$  mas in Table 1 of Reid et al. 2014). Due to the close correspondence between the molecular gas and the maser source, we suggest that the northern and southwestern MCs in the interval of  $V_{\text{LSR}} \sim 42\text{--}48 \text{ km s}^{-1}$  (and their associated OB stars, see red crosses in Figure 19) are at the same distance of 4–5 kpc. Accordingly, SNR G213.0–0.6 has no connection to H II region Sh 2-284 (and the  $V_{\text{LSR}} \sim 28 \text{ km s}^{-1}$  MCs) because of their different distances.

#### 4. SUMMARY

A large-scale CO survey has been performed with high spatial ( $\sim 50''$ ) and velocity ( $\sim 0.2 \text{ km s}^{-1}$ ) resolution to study the molecular environment of SNRs G205.5+0.5, G206.9+2.3, and G213.0–0.6. The high-quality CO data reveal complex structures in the molecular gas toward the three remnants. The resulting CO maps also allow us to investigate in detail the relationship between the SNRs and the molecular gas. We summarize our main results as follows.

1. SNR G205.5+0.5 is actually associated with the MCs at  $V_{\text{LSR}} \sim 5 \text{ km s}^{-1}$  and  $19 \text{ km s}^{-1}$ . The  $5 \text{ km s}^{-1}$  molecular gas, which exhibits the blueshifted CO broadening, is identified to be connected with obscuring optical regions. Whereas the  $19 \text{ km s}^{-1}$  MCs with redshifted line-broadening are on the farside of the remnant. On the other hand, the nearby Rosette Nebula is also physically related to these two

MC components, suggesting the association between the Nebula and the SNR. Using the 3D extinction map from Green et al. (2015), the distances of the two molecular components are estimated to be  $\sim 1.6$  kpc for the  $5 \text{ km s}^{-1}$  MCs and  $\sim 1.6\text{--}2.0$  kpc for the  $19 \text{ km s}^{-1}$  MCs, which agree well with the distance of  $\sim 1.6$  kpc from the connection between the SNR and the Rosette Nebula. The confirmation of SNR–MC interaction toward SNR G205.5+0.5 supports the hadronic origin of the extended gamma-ray emission inside the remnant.

2. SNR G213.0–0.6 is interacting with the  $8\text{--}11 \text{ km s}^{-1}$  MCs. Based on the 3D extinction map from Green et al. (2015), the SNR’s distance is  $\sim 1$  kpc from that of the associated molecular gas, which is consistent well with the estimates from the updated  $\Sigma$ – $D$  relationship (Pavlovic et al. 2014) and the kinematic distance inferred from the LSR velocity of  $8\text{--}11 \text{ km s}^{-1}$ . The remnant has no relation to the southwestern H II region Sh 2-284, which is located at a distance of  $4\text{--}5$  kpc.

3. For SNR G206.9+2.3, we notice that this remnant seems to be located in a molecular cavity at  $\sim 15 \text{ km s}^{-1}$ . Moreover, a partial shell structure at  $V_{\text{LSR}} \sim 14\text{--}15 \text{ km s}^{-1}$  is found to be expanding outward at the southeastern boundary of the remnant. While this evidence may indicate an association between the SNR and the molecular gas, no significant molecular line

broadening has been obtained. If the SNR–MC association is true, the kinematic distance to SNR G206.9+2.3 is  $\sim 1.6$  kpc.

4. SNRs G205.5+0.5 and G213.0–0.6 evolved in the low-density environment and are now interacting with their ambient molecular gas. However, SNR G206.9+2.3 seems to be still evolving in the molecular cavity. The SNRs’ low-density environment may be created by their progenitors’ activities. These SNRs are a good laboratory for establishing the relationships between SNRs and their environments because of their large angular sizes, relatively near distances, and likely SNR–MC interaction. Detailed analyses and discussions will be valuable for understanding the remnant’s evolution and the interaction of SNRs with their surroundings through further multiwavelength studies.

The authors acknowledge the staff members of the Qinghai Radio Observing Station at Delingha for their support of the observations. We would like to thank the anonymous referee for valuable comments and suggestions that helped to improve this paper. This work is supported by NSFC grants 11233001 and 11233007. X.Z. acknowledges support by NSFC grant 11403104 and Jiangsu Provincial Natural Science Foundation grant BK20141044. Y.C. acknowledges support by 973 Program grant 2015CB857100 and NSFC grant 11633007. Y.L. acknowledges support by NSFC grant 11233006.

## REFERENCES

- Aharonian, F. A., Akhperjanian, A. G., Bazer-Bachi, A. R., et al. 2007, *A&A*, 469, L1
- Ambrocio-Cruz, P., Rosado, M., Le Coarer, E., Bernal, A., & Gutiérrez, L. 2014, *RMxAA*, 50, 323
- Anderl, S., Gusdorf, A., & Güsten, R. 2014, *A&A*, 569, A81
- Baxter, E. J., Covey, K. R., Muench, A. A., et al. 2009, *AJ*, 138, 963
- Bolatto, A. D., Wolfire, M., & Leroy, A. K. 2013, *ARA&A*, 51, 207
- Casandjian, J.-M., & Grenier, I. A. 2008, *A&A*, 489, 849
- Chen, X., Xiong, F., & Yang, J. 2016, arXiv160805329C, arXiv:1608.05329
- Chen, Y., Jiang, B., Zhou, P., et al. 2014, in IAU Symposium, Vol. 296, Supernova Environmental Impacts, ed. A. Ray & R. A. McCray, 170–177
- Chevalier, R. A. 1974, *ApJ*, 188, 501

- Condon, J. J., Griffith, M. R., & Wright, A. E. 1993, AJ, 106, 1095
- Cusano, F., Ripepi, V., Alcalá, J. M., et al. 2011, MNRAS, 410, 227
- Davies, R. D., Elliott, K. H., Goudis, C., Meaburn, J., & Tebbutt, N. J. 1978, A&AS, 31, 271
- Delgado, A. J., Djupvik, A. A., & Alfaro, E. J. 2010, A&A, 509, A104
- Dent, W. R. F., Hovey, G. J., Dewdney, P. E., et al. 2009, MNRAS, 395, 1805
- Dickel, J. R., & Denoyer, L. K. 1975, AJ, 80, 437
- Dirks, C., & Meyer, D. M. 2016, ApJ, 819, 45
- Dubner, G., & Giacani, E. 2015, A&A Rv, 23, 3
- Fesen, R. A., Blair, W. P., & Kirshner, R. P. 1985, ApJ, 292, 29
- Fujita, Y., Ohira, Y., Tanaka, S. J., & Takahara, F. 2009, ApJL, 707, L179
- Furst, E., Reich, W., Reich, P., & Reif, K. 1990, A&AS, 85, 691
- Gao, X. Y., Han, J. L., Reich, W., et al. 2011, A&A, 529, A159
- Graham, D. A., Haslam, C. G. T., Salter, C. J., & Wilson, W. E. 1982, A&A, 109, 145
- Green, D. A. 2014, Bulletin of the Astronomical Society of India, 42, 47
- Green, G. M., Schlafly, E. F., Finkbeiner, D. P., et al. 2015, ApJ, 810, 25
- Hartman, R. C., Bertsch, D. L., Bloom, S. D., et al. 1999, ApJS, 123, 79
- Hensberge, H., Pavlovski, K., & Verschueren, W. 2000, A&A, 358, 553
- Huang, Y.-L., & Thaddeus, P. 1986, ApJ, 309, 804
- Jeong, I.-G., Byun, D.-Y., Koo, B.-C., et al. 2012, Ap&SS, 342, 389
- Jiang, B., Chen, Y., Wang, J., et al. 2010, ApJ, 712, 1147
- Kamezaki, T., Imura, K., Omodaka, T., et al. 2014, ApJS, 211, 18
- Katagiri, H., Sugiyama, S., Ackermann, M., et al. 2016, ApJ, 831, 106
- Kilpatrick, C. D., Bieging, J. H., & Rieke, G. H. 2014, ApJ, 796, 144
- . 2016, ApJ, 816, 1
- Lasker, B. M., Sturch, C. R., McLean, B. J., et al. 1990, AJ, 99, 2019
- Leahy, D. A. 1986, A&A, 156, 191
- Leahy, D. A., Narayan, S., & Singh, K. P. 1985, MNRAS, 213, 15P
- . 1986, MNRAS, 220, 501
- McKee, C. F., & Cowie, L. L. 1975, ApJ, 195, 715
- Negueruela, I., Simón-Díaz, S., Lorenzo, J., Castro, N., & Herrero, A. 2015, A&A, 584, A77
- Nolan, P. L., Abdo, A. A., Ackermann, M., et al. 2012, ApJS, 199, 31
- Odegard, N. 1986, ApJ, 301, 813
- Oliver, R. J., Masheder, M. R. W., & Thaddeus, P. 1996, A&A, 315, 578
- Park, B.-G., & Sung, H. 2002, AJ, 123, 892
- Parker, Q. A., Phillipps, S., Pierce, M. J., et al. 2005, MNRAS, 362, 689
- Paron, S., Celis Peña, M., Ortega, M. E., et al. 2015, A&A, 580, A51
- Pavlovic, M. Z., Dobardzic, A., Vukotic, B., & Urosevic, D. 2014, Serbian Astronomical Journal, 189, 25
- Reich, P., Reich, W., & Furst, E. 1997, A&AS, 126, doi:10.1051/aas:1997274
- Reich, W., Zhang, X., & Fürst, E. 2003, A&A, 408, 961
- Reid, M. J., Menten, K. M., Brunthaler, A., et al. 2014, ApJ, 783, 130
- Rho, J., Hewitt, J. W., Bieging, J., et al. 2017, ApJ, 834, 12
- Sano, H., Nakamura, K., Furukawa, N., et al. 2016, arXiv160607745S, arXiv:1606.07745
- Schneider, N., Stutzki, J., Winnewisser, G., & Block, D. 1998, A&A, 335, 1049
- Shan, W. L., Yang, J., Shi, S. C., et al. 2012, IEEE Transactions on Terahertz Science and Technology, 2, 593
- Slane, P., Bykov, A., Ellison, D. C., Dubner, G., & Castro, D. 2015, SSRv, 188, 187
- Stupar, M., & Parker, Q. A. 2012, MNRAS, 419, 1413
- Su, Y., Fang, M., Yang, J., Zhou, P., & Chen, Y. 2014a, ApJ, 788, 122
- Su, Y., Yang, J., Zhou, X., Zhou, P., & Chen, Y. 2014b, ApJ, 796, 122
- Sung, H., Bessell, M. S., & Lee, S.-W. 1997, AJ, 114, 2644
- Wallerstein, G., & Jacobsen, T. S. 1976, ApJ, 207, 53
- Welsh, B. Y., Sfeir, D. M., Sallmen, S., & Lallement, R. 2001, A&A, 372, 516
- Xiao, L., & Zhu, M. 2012, A&A, 545, A86
- Yamazaki, R., Kohri, K., Bamba, A., et al. 2006, MNRAS, 371, 1975
- Zhou, P., Chen, Y., Zhang, Z.-Y., et al. 2016a, ApJ, 826, 34

- Zhou, X., Yang, J., Fang, M., & Su, Y. 2014, ApJ, 791, 109
- Zhou, X., Yang, J., Fang, M., et al. 2016b, ApJ, 833, 4

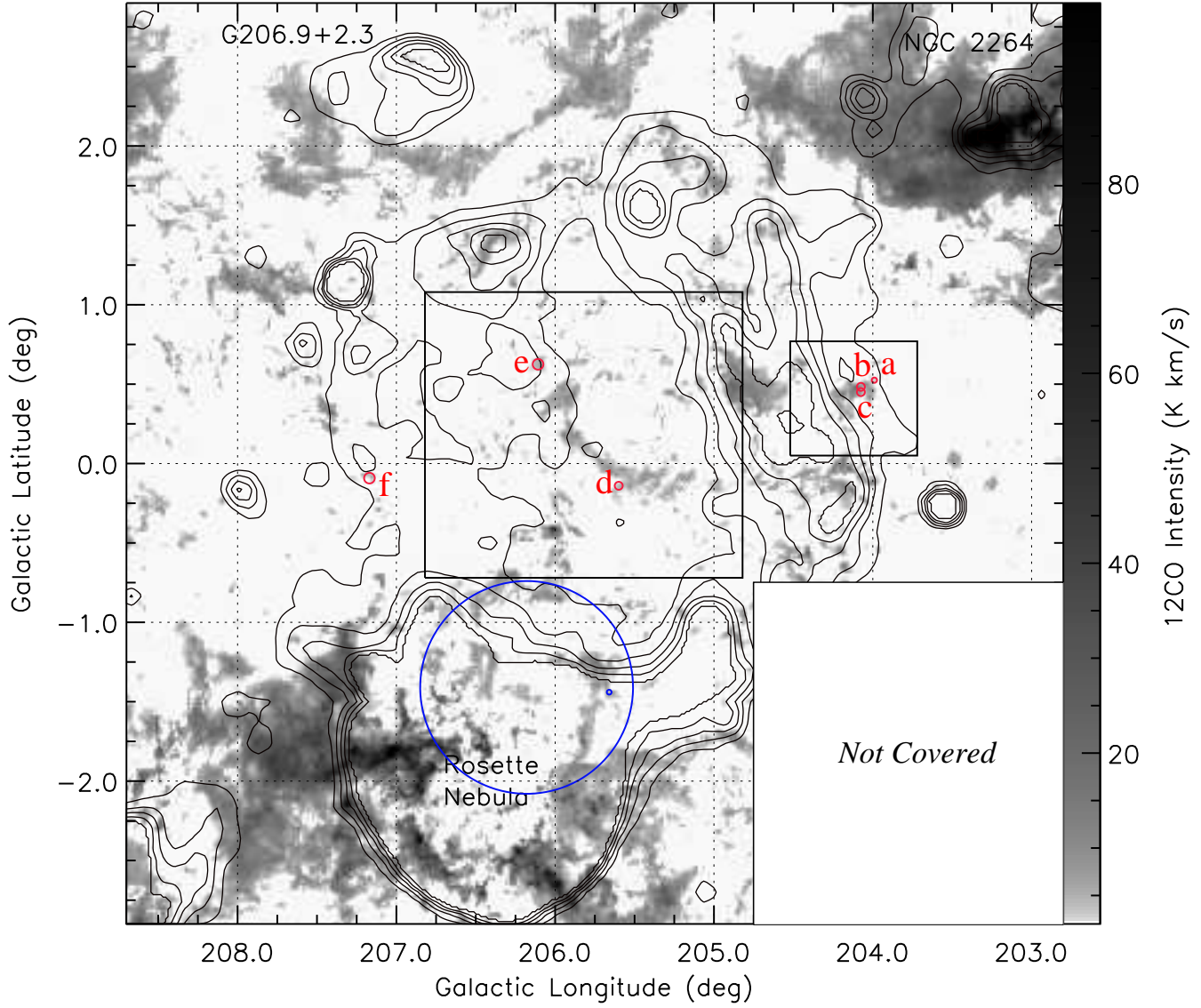


**Figure 1.** Integrated  $^{12}\text{CO}$  ( $J=1-0$ ) emission toward SNR G205.5+0.5 from  $-10$  to  $50$   $\text{km s}^{-1}$ , overlaid with radio continuum contours from the Effelsberg 21 cm survey (Reich et al. 1997). The radio contour levels are at  $340$ ,  $480$ ,  $620$ ,  $760$ , and  $900$  mK. The two rectangles indicate regions shown in Figures 2 and 6, respectively. Six red circles, which are denoted with letters a-f, indicate positions of shocked gas (see spectra in Figure 8). Sizes of these red circles are enlarged to two times with respect to their angular sizes ( $1'$ - $2'$ ). The nearby sources of NGC 2264 and Rosette Nebula, as well as SNR G206.9+2.3, are also labeled. The little and large blue circles indicate the point TeV source, HESS J0632+057 (Aharonian et al. 2007), and extended or confused source, 3EG J0634+0521 (Hartman et al. 1999; Casandjian & Grenier 2008), respectively.

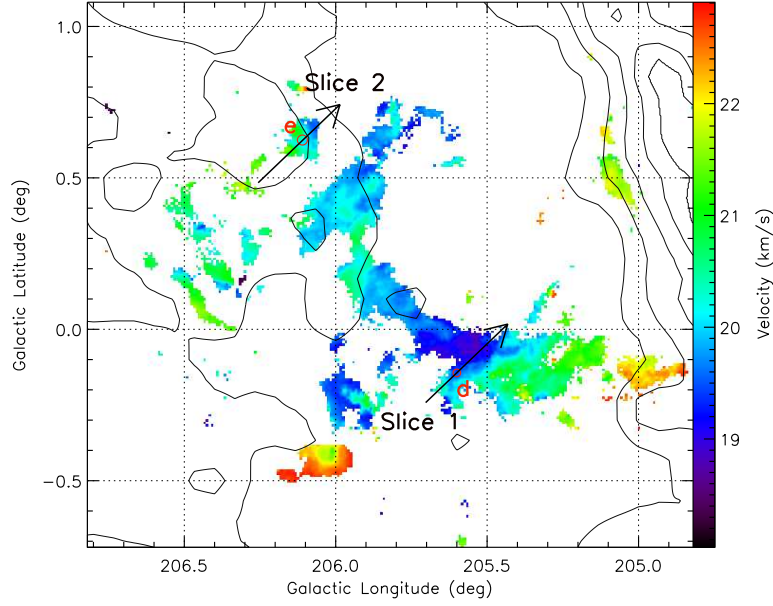


**Figure 2.** Intensity-weighted  $^{12}\text{CO}$  ( $J=1-0$ ) mean velocity (first moment) map of MCs toward the center of SNR G205.5+0.5 in the interval of 18–23 km  $\text{s}^{-1}$ , overlaid with the same radio contours as in Figure 1. The two arrows of Slice 1 and Slice 2 indicate the PV slice shown in Figure 3. Positions and sizes of shocked gas (see spectra in Figure 8) are also labeled.

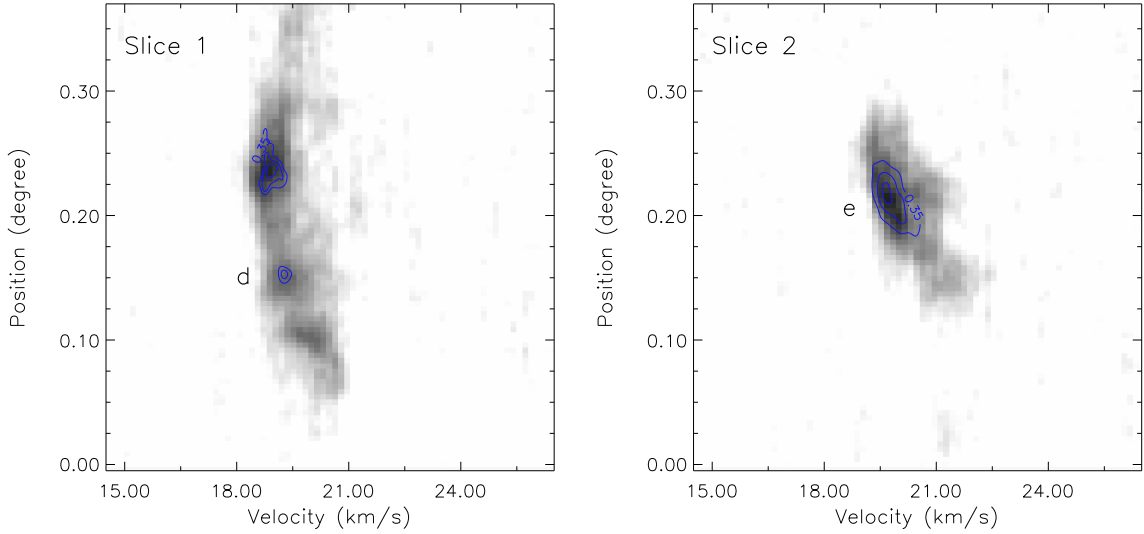


**Figure 3.** Left panel: PV diagram of  $^{12}\text{CO}$  ( $J=1-0$ ) emission along slice 1, overlaid with the blue contours of  $^{13}\text{CO}$  emission. The overlaid contours levels are at 0.35 ( $3\sigma$ ), 0.47, and 0.58 K. The PV slice has a length of  $22.5'$  (from  $(l = 205^\circ.703, b = -0^\circ.242)$  to  $(l = 205^\circ.432, b = 0^\circ.017)$ ) and a width of  $2.5'$  (see the arrow slice 1 in Figure 2). Right panel: PV diagram of  $^{12}\text{CO}$  ( $J=1-0$ ) emission along slice 1, overlaid with the blue contours of  $^{13}\text{CO}$  emission. The overlaid contours levels are at 0.35 ( $3\sigma$ ), 0.70, and 1.05 K. The PV slice has a length of  $22.5'$  (from  $(l = 206^\circ.256, b = 0^\circ.484)$  to  $(l = 205^\circ.986, b = 0^\circ.742)$ ) and a width of  $2.5'$  (see the arrow slice 2 in Figure 2).

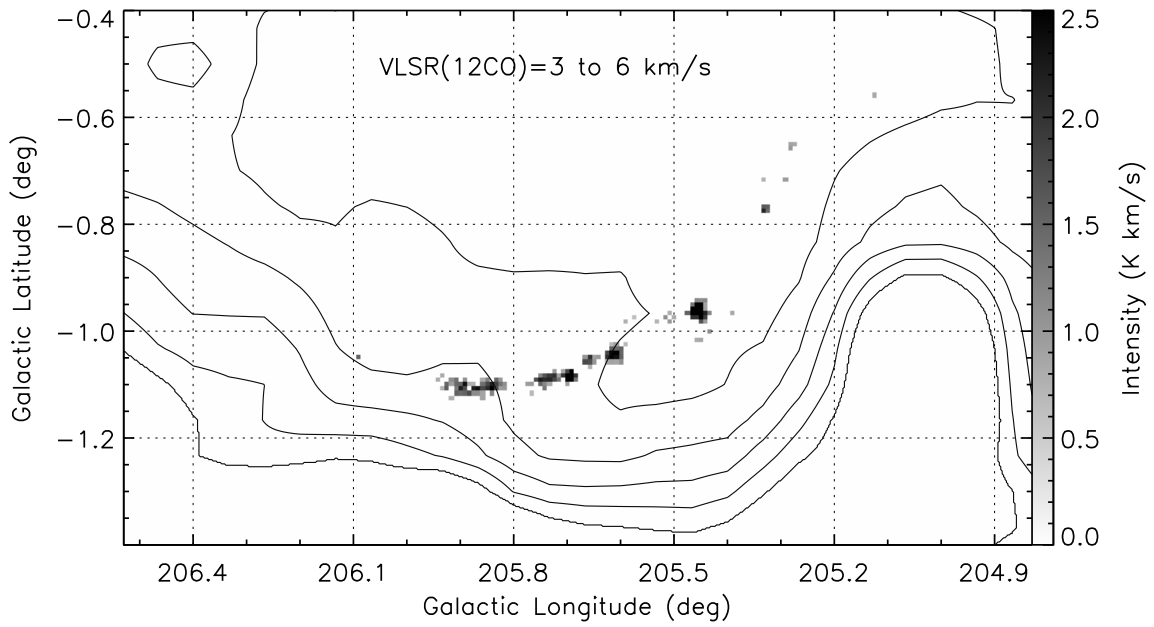


**Figure 4.** Integrated  $^{12}\text{CO}$  ( $J=1-0$ ) emission toward the southwestern boundary of SNR G205.5+0.5 from 3 to 6  $\text{km s}^{-1}$ , overlaid with the same radio contours as in Figure 1.

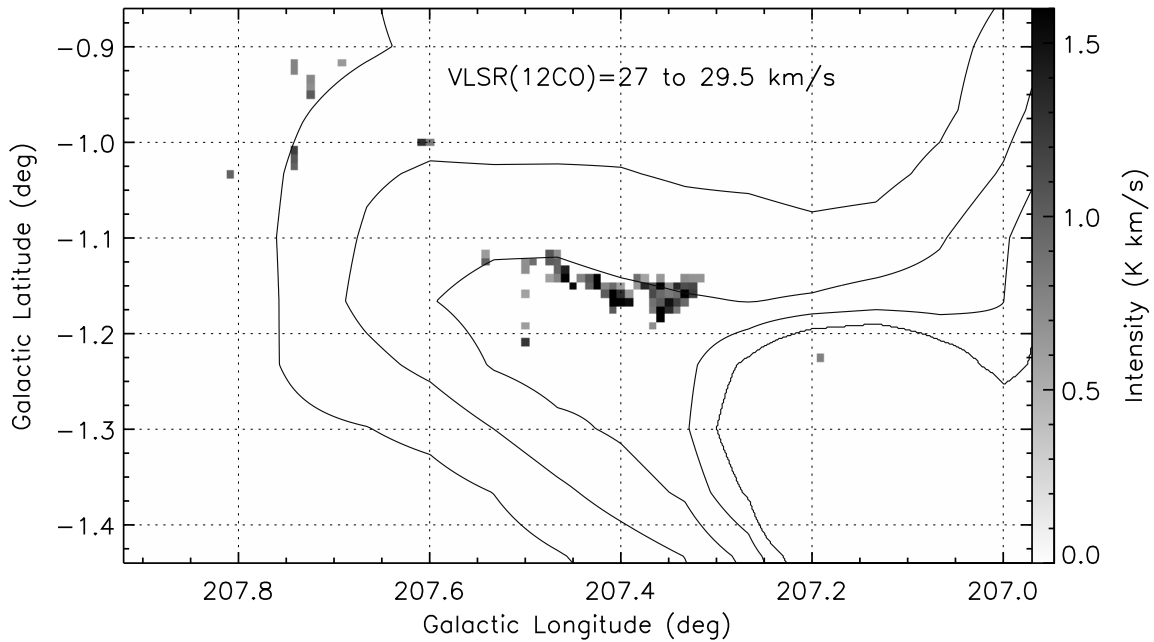


**Figure 5.** Integrated  $^{12}\text{CO}$  ( $J=1-0$ ) emission toward the southeastern shell of SNR G205.5+0.5 from 27 to 29.5  $\text{km s}^{-1}$ , overlaid with the same radio contours as in Figure 1.

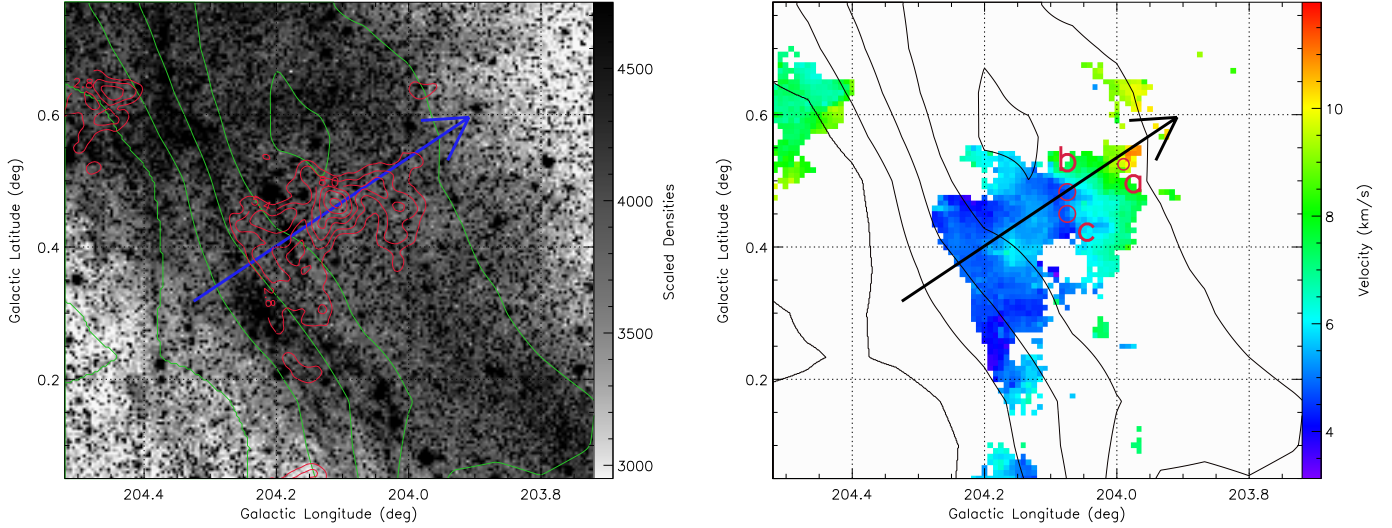


**Figure 6.** Left panel: optical image (the Digitized Sky Survey, Lasker et al. 1990) toward the western boundary of SNR G205.5+0.5, overlaid with green radio contours as in Figure 1. Red contours show the  $^{12}\text{CO}$  ( $J=1-0$ ) distribution (in units of  $\text{K km s}^{-1}$ ) integrated from 3 to 12  $\text{km s}^{-1}$ . The arrow indicates the PV slice shown in Figure 7. Right panel: intensity-weighted  $^{12}\text{CO}$  ( $J=1-0$ ) mean velocity (first moment) map of MCs in the interval of 3–12  $\text{km s}^{-1}$ , overlaid with the same radio contours as in the left panel. Positions and sizes of shocked gas (see spectra in Figure 8) are also labeled.

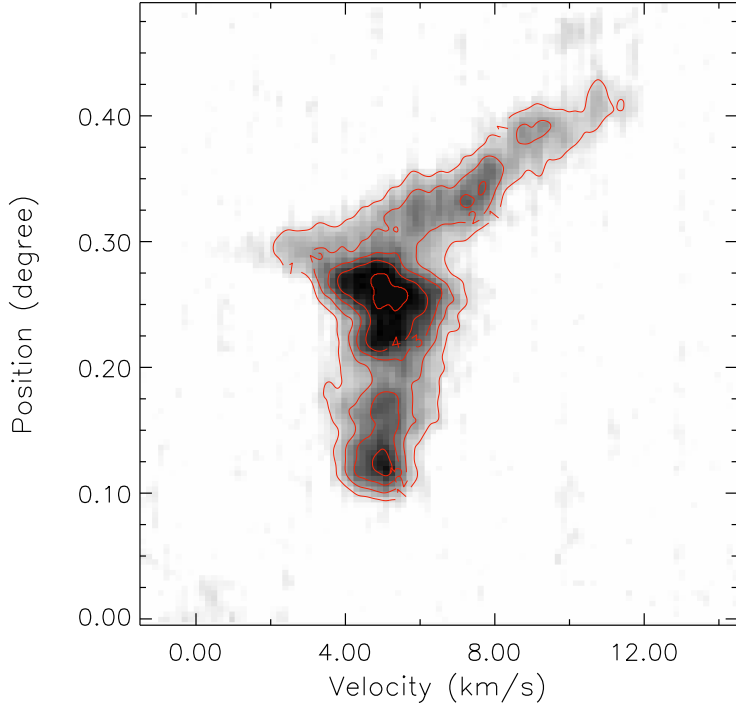


**Figure 7.** PV diagram of  $^{12}\text{CO}$  ( $J=1-0$ ) emission in the western radio boundary of SNR G205.5+0.5 (see the right rectangle in Figure 1). The PV slice with a length of 30' (from  $(l = 204^\circ 325, b = 0^\circ 318)$  to  $(l = 203^\circ 909, b = 0^\circ 596)$ ) and a width of 2'5 is just perpendicular to the SNR's radio shell (see the arrow in Figure 6). The red contours indicate the emission of  $^{12}\text{CO}$  in units of K.

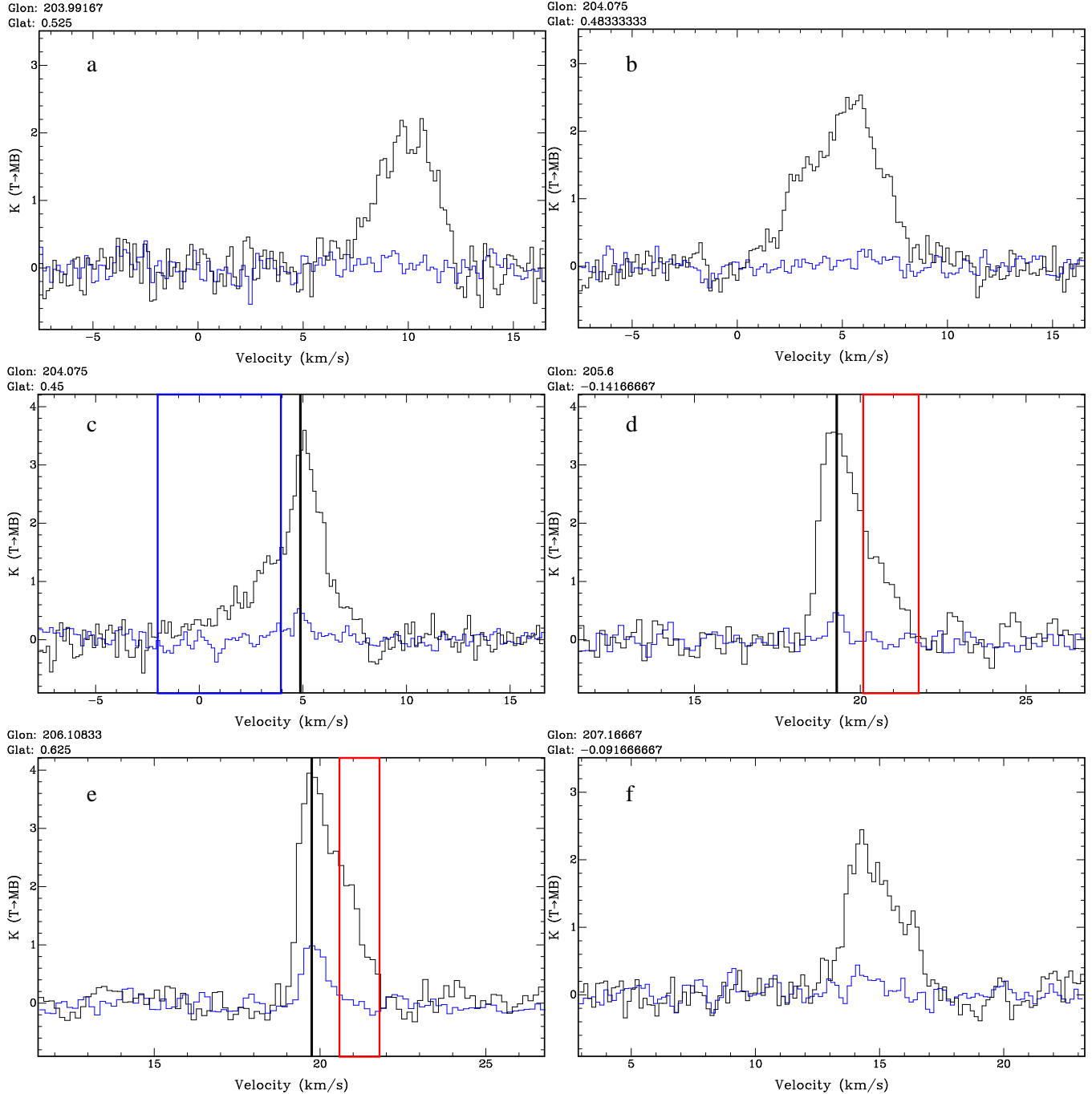


**Figure 8.**  $^{12}\text{CO}$  ( $J=1-0$ ; black) and  $^{13}\text{CO}$  ( $J=1-0$ ; blue) spectra of shocked gas toward SNR G205.5+0.5. Positions of shocked MCs are labeled in Figure 1. These spectra are extracted from regions of  $1 \times 1$ ,  $1.5 \times 1.5$ ,  $1.5 \times 1.5$ ,  $1.5 \times 1.5$ ,  $2 \times 2$ , and  $2 \times 2$  arcmin $^2$  for points a–f, respectively. The solid lines indicate the LSR velocity of unperturbed clouds from the  $^{13}\text{CO}$  peak. The red and blue rectangles show the velocity range of the wing from  $^{12}\text{CO}$  emission, which indicates the shocked gas. Note that only selected typical spectra with relatively prominent asymmetric line structures are shown in the Figure.

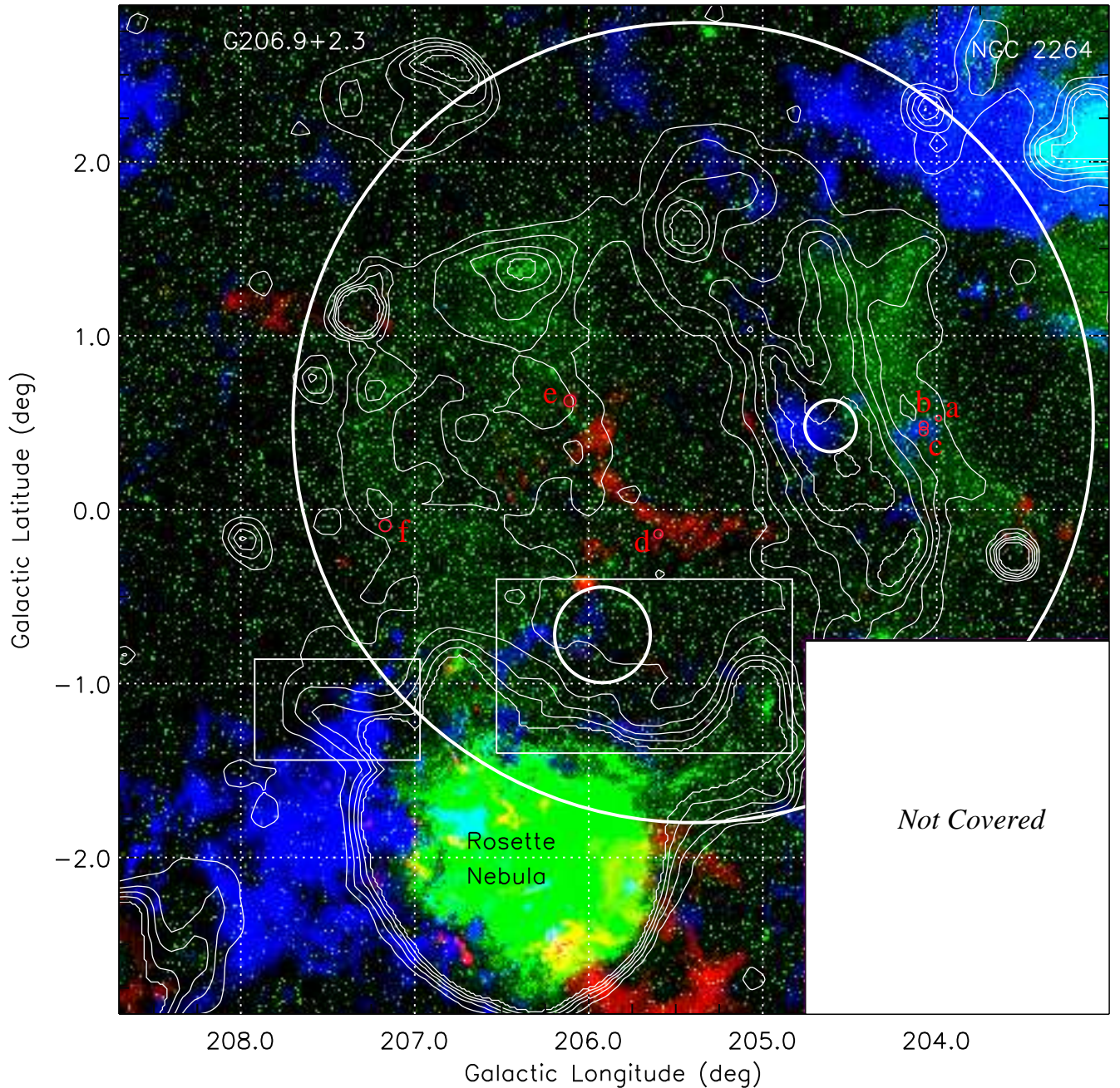


**Figure 9.** Integrated  $^{12}\text{CO}$  ( $J=1-0$ ) emission toward SNR G205.5+0.5 in the interval of 3–12 km s $^{-1}$  (blue) and 18–23 km s $^{-1}$  (red), overlaid with the same radio contours as in Figure 1. The optical emission is shown in green. The two rectangles indicate regions shown in Figures 4 and 5, respectively. Sizes of the red circles are enlarged to two times with respect to their angular sizes (1'–2'). The large white circle indicates the best-fit Gaussian spatial model from *FERMI/LAT* observations after subtracting the background and the emission from the Rosette Nebula (Katagiri et al. 2016), while the two little white circles show the 2FGL sources of J0636.0+0554 and J0637.8+0737 (Nolan et al. 2012).

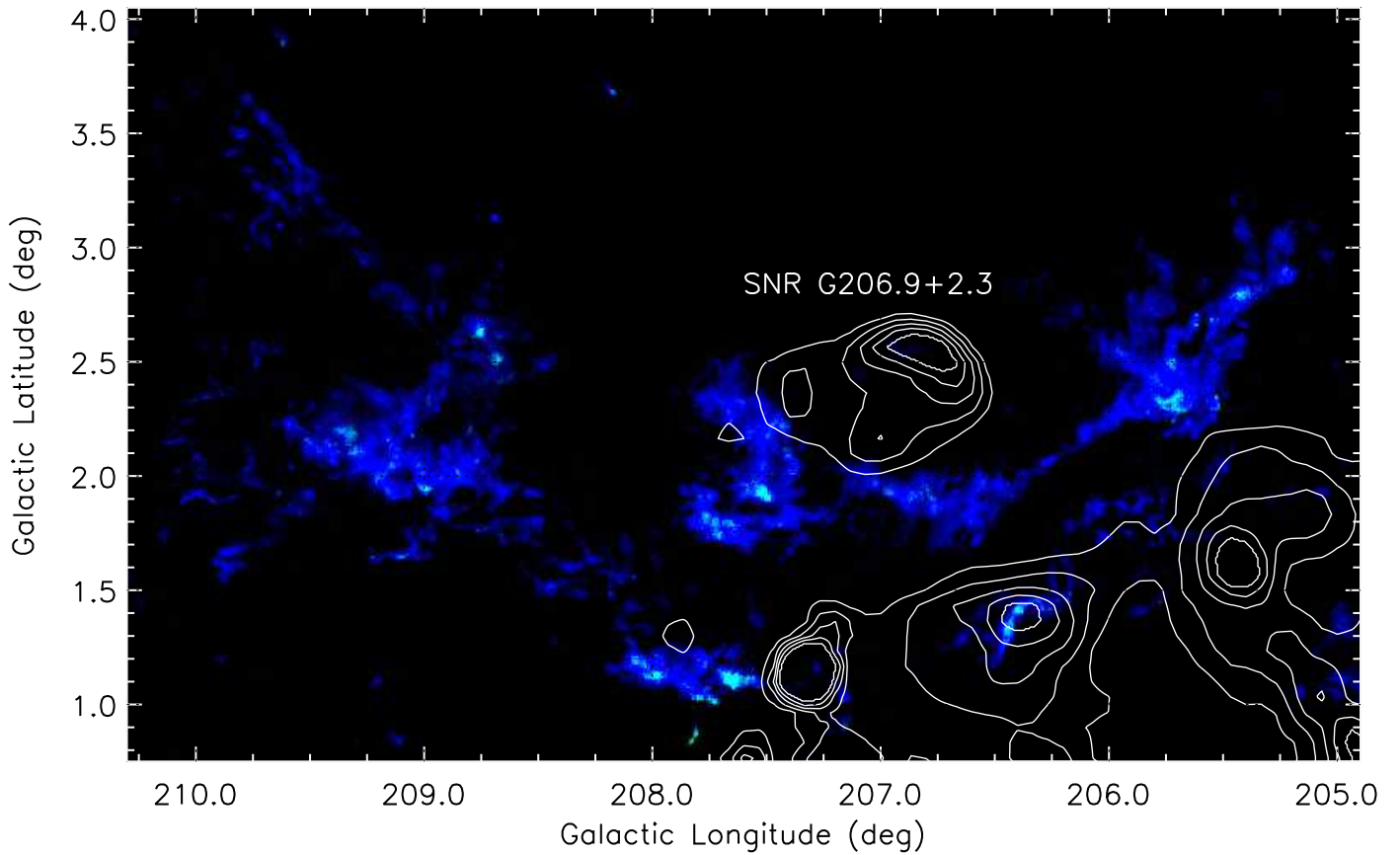


**Figure 10.**  $^{12}\text{CO}$  ( $J=1-0$ , blue) and  $^{13}\text{CO}$  ( $J=1-0$ , green) intensity map toward G206.9+2.3 in the 11–19  $\text{km s}^{-1}$  interval, overlaid with radio continuum contours from the Effelsberg 21 cm survey (Reich et al. 1997). The radio contours levels are at 340, 480, 620, 760, and 900 mK.

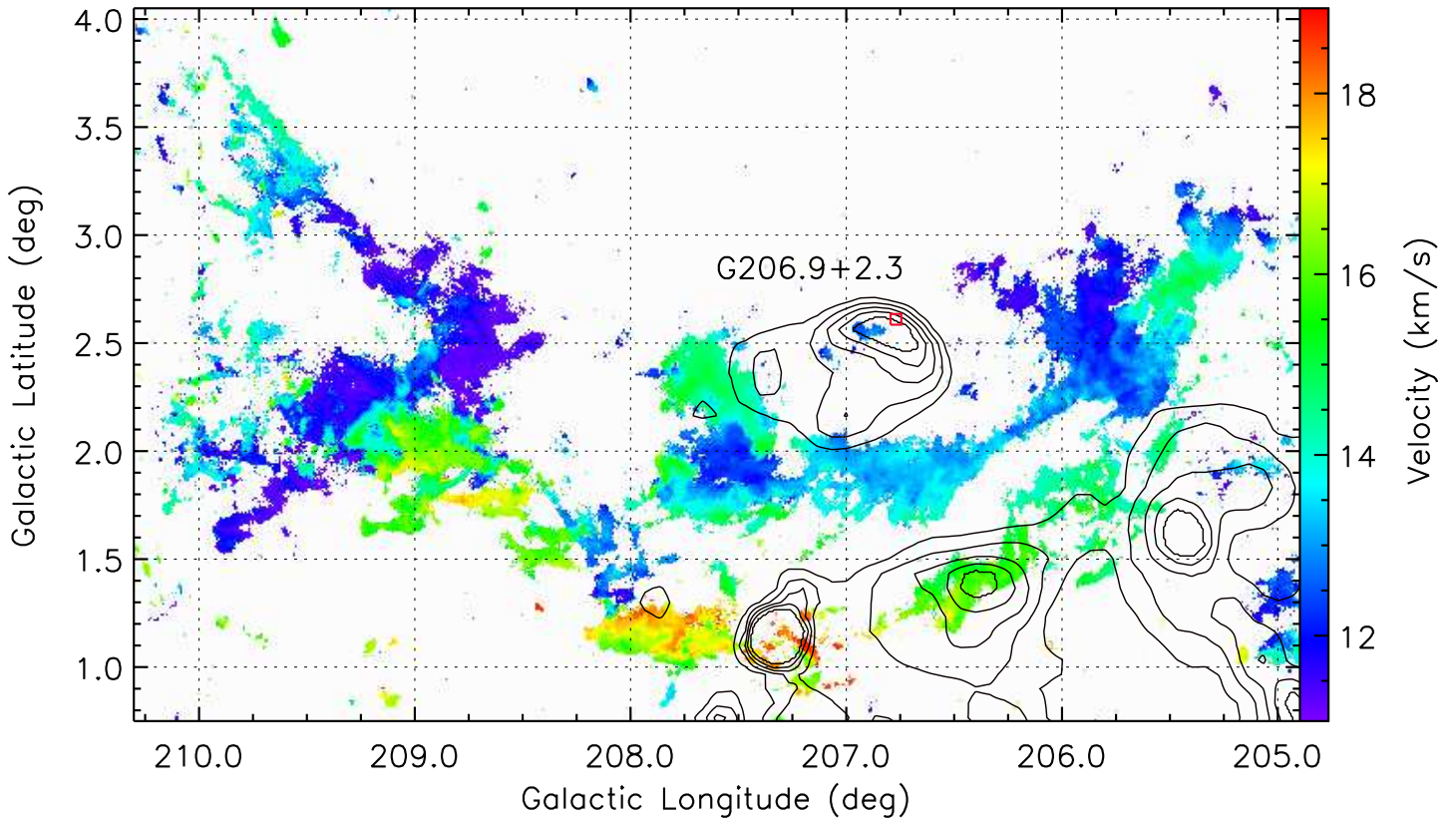


**Figure 11.** Intensity-weighted  $^{12}\text{CO}$  ( $J=1-0$ ) mean velocity (first moment) map of MCs toward SNR G206.9+2.3 in the interval of  $11\text{--}19\text{ km s}^{-1}$ , overlaid with the same radio contours as in Figure 10. The red box indicates position 1 in [Fesen et al. \(1985\)](#).

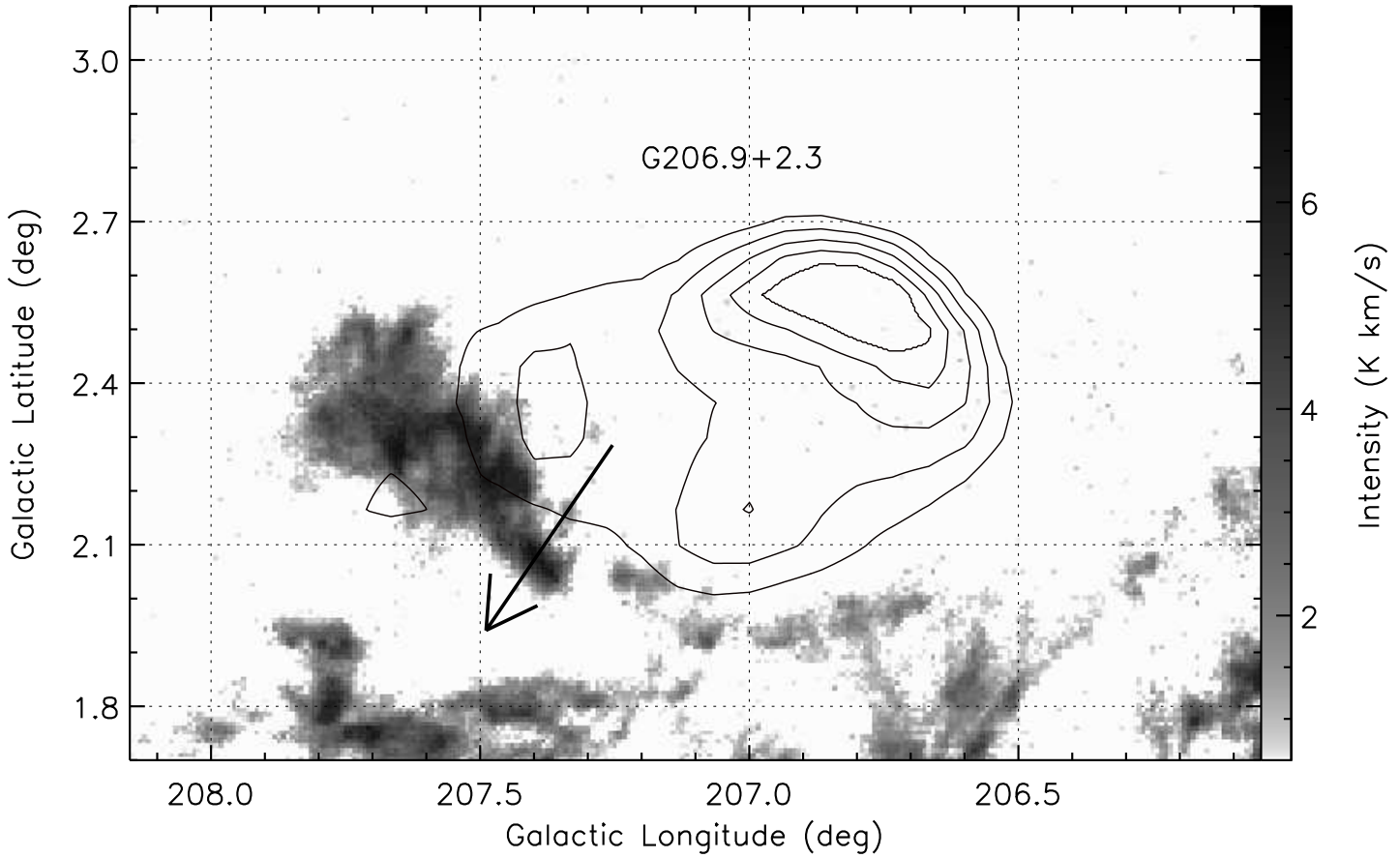


**Figure 12.** Integrated  $^{12}\text{CO}$  ( $J=1-0$ ) emission toward SNR G206.9+2.3 from 14 to 15  $\text{km s}^{-1}$ , overlaid with the same contours as in Figure 10. The square-root scale is used to enhance the faint CO emission along the southern boundary of the remnant.

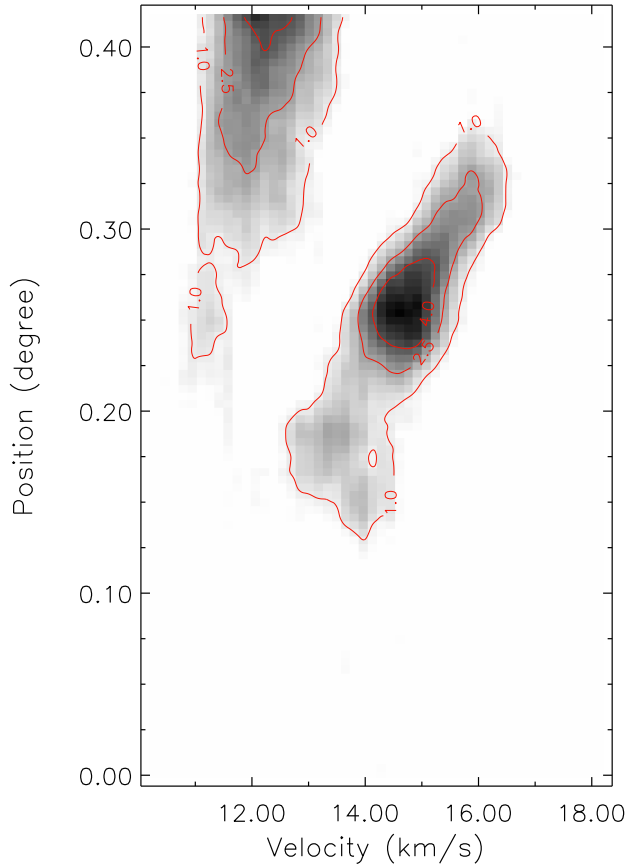


**Figure 13.** PV diagram of  $^{12}\text{CO}$  ( $J=1-0$ ) emission in the southeast of SNR G206.9+2.3. The PV slice with length of  $25'$  (from  $(l = 207^\circ.254, b = 2^\circ.285)$  to  $(l = 207^\circ.489, b = 1^\circ.941)$ ) and width of  $4.5'$  is perpendicular to the SNR's radio shell and the MC partial shell structures (see the arrow in Figure 12). The red contours indicate the emission of  $^{12}\text{CO}$  in units of K.

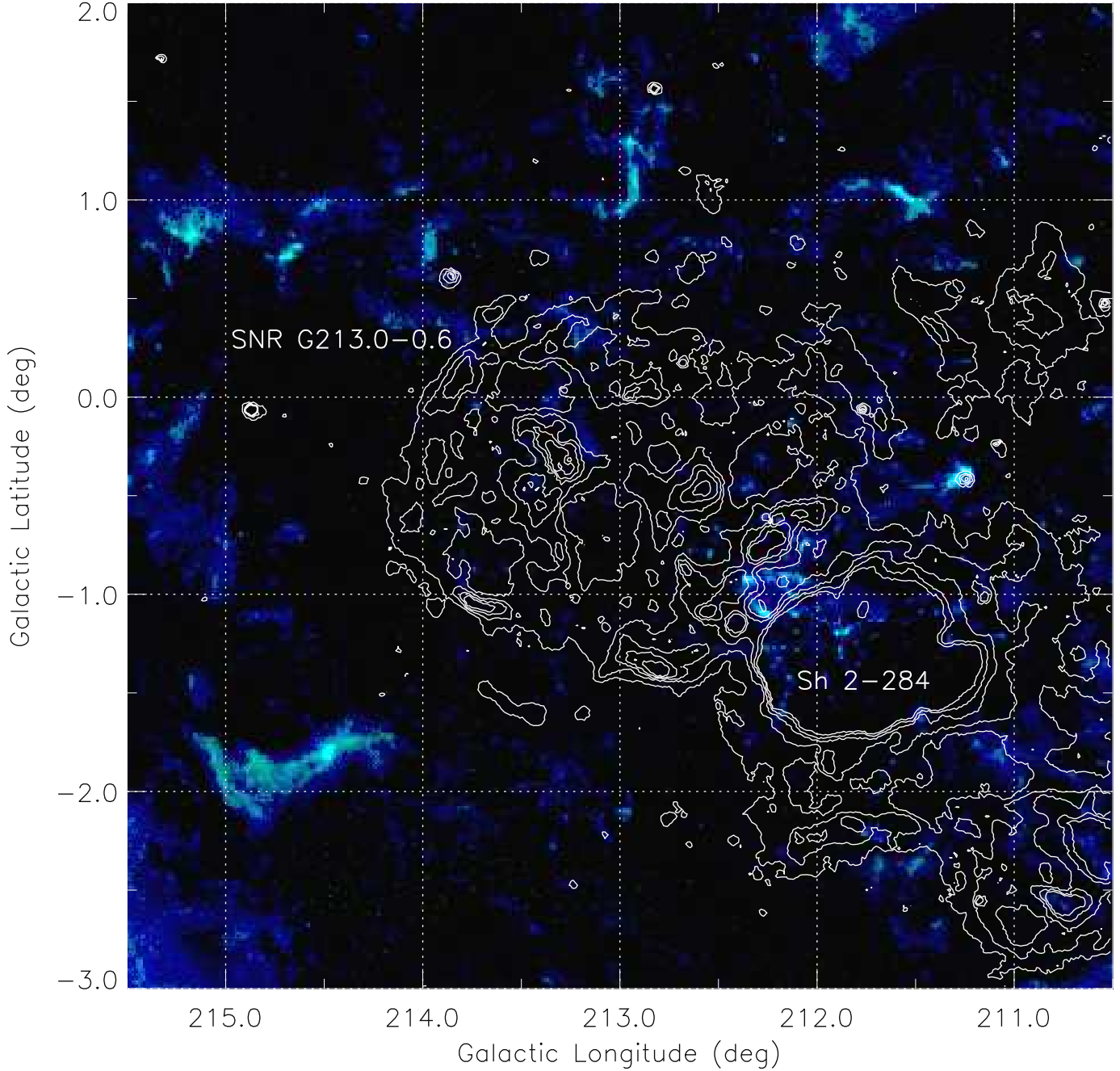


**Figure 14.**  $^{12}\text{CO}$  ( $J=1-0$ ; blue) and  $^{13}\text{CO}$  ( $J=1-0$ ; green) intensity map toward SNR G213.0–0.6 in the 0–60  $\text{km s}^{-1}$  interval, overlaid with optical contours from the Southern H $\alpha$  Sky Survey (Parker et al. 2005). The SHASSA contour levels are at 220, 296, 372, 448, and 524 decirayleighs. The HII region Sh 2-284 is also labeled in the lower-right corner.

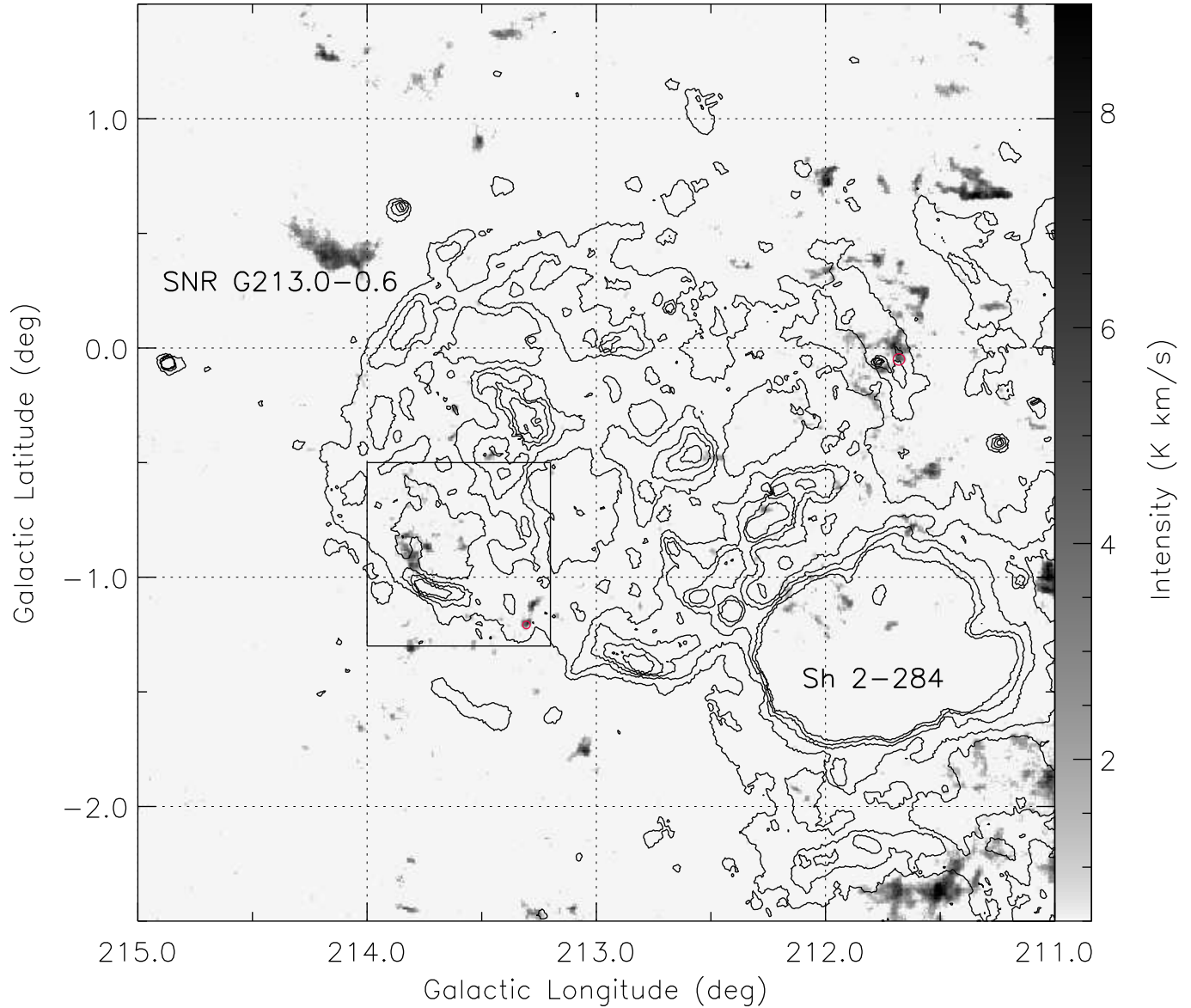


**Figure 15.** Integrated  $^{12}\text{CO}$  ( $J=1-0$ ) emission toward SNR G213.0–0.6 from 2 to 15  $\text{km s}^{-1}$ , overlaid with the same contours as in Figure 14. The box indicates the region shown in Figure 16. Two red circles indicate positions of shocked gas, of which spectra are shown in Figure 18.

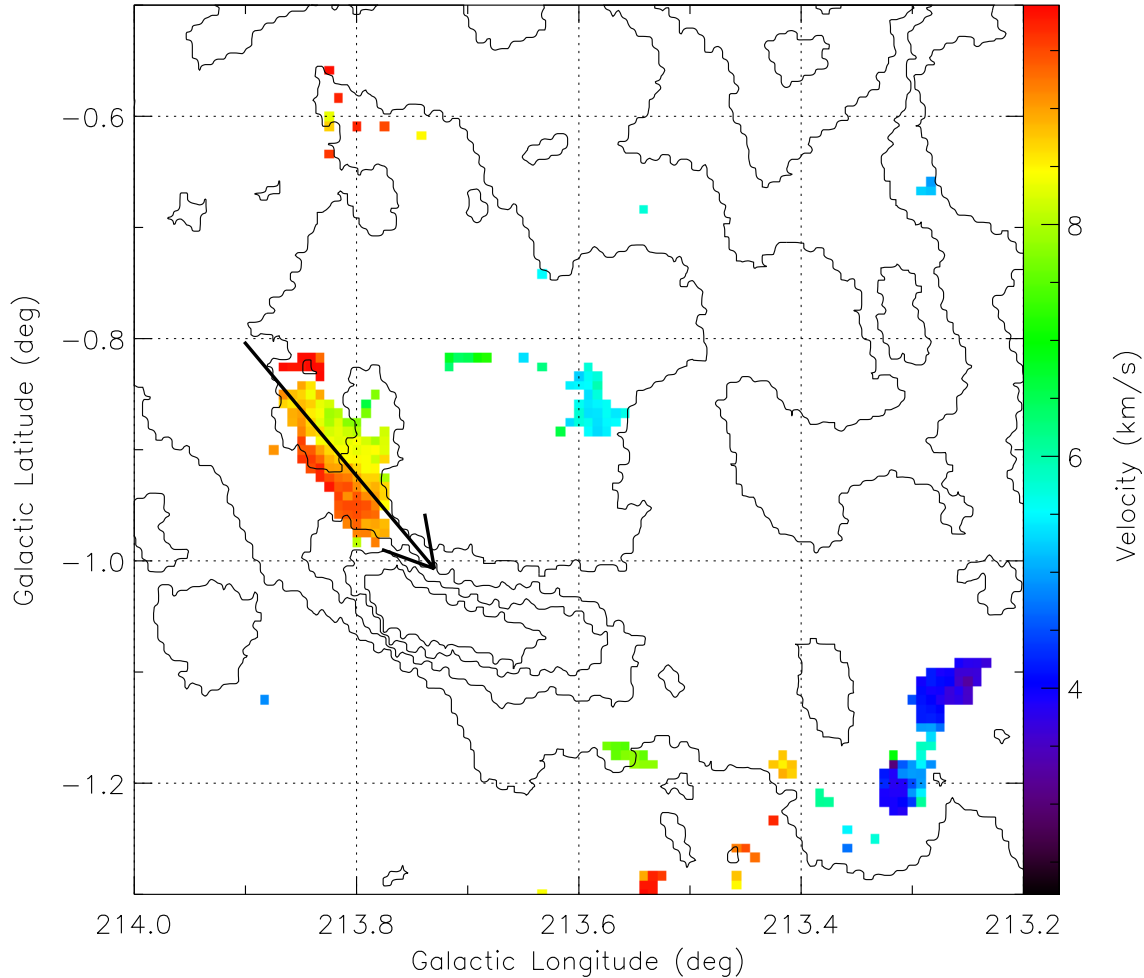


**Figure 16.** Intensity-weighted  $^{12}\text{CO}$  ( $J=1-0$ ) mean velocity (first moment) map of MCs in the interval of  $2-10 \text{ km s}^{-1}$ , overlaid with the same contours as in Figure 14. The arrow indicates the PV slice shown in Figure 17.

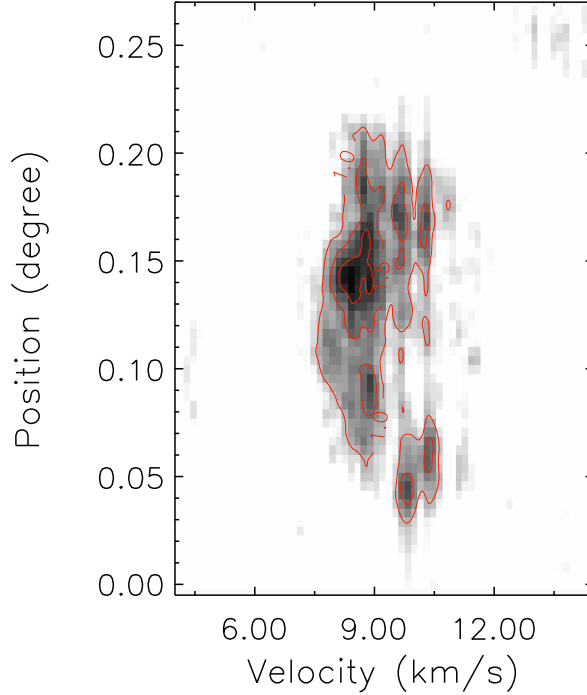


**Figure 17.** PV diagram of  $^{12}\text{CO}$  ( $J=1-0$ ) emission near the  $\text{H}\alpha$  peak of SNR G213.0–0.6’s southeastern boundary (see Figure 5a in Stupar & Parker 2012). The PV slice with a length of  $16'$  (from  $(l = 213^\circ.901, b = -0^\circ.803)$  to  $(l = 213^\circ.730, b = -1^\circ.007)$ ) and a width of  $4'5$  is along the SNR’s radio shell (see the arrow in Figure 17). The red contours indicate the emission of  $^{12}\text{CO}$  in units of K.

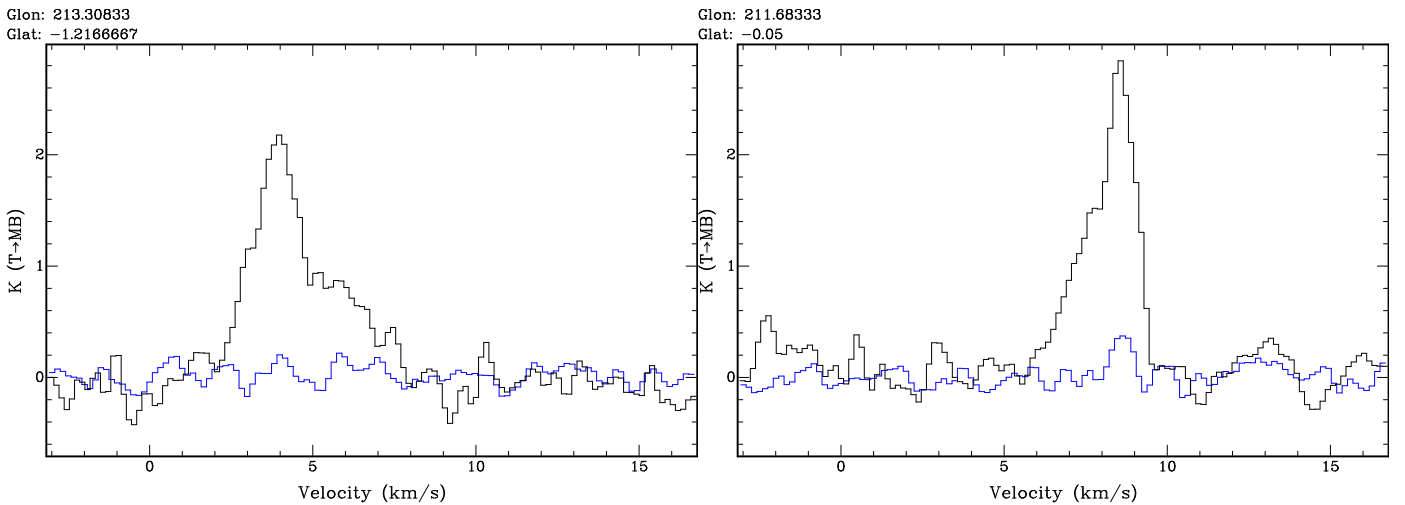


**Figure 18.**  $^{12}\text{CO}$  ( $J=1-0$ ; black) and  $^{13}\text{CO}$  ( $J=1-0$ ; blue) spectra of the shocked gas toward SNR G213.0–0.6. The two positions of the shocked MCs are labeled red circles in Figure 15. The two spectra are extracted from regions of  $2 \times 2$  and  $3 \times 2$  arcmin $^2$  for the left panel and the right panel, respectively.

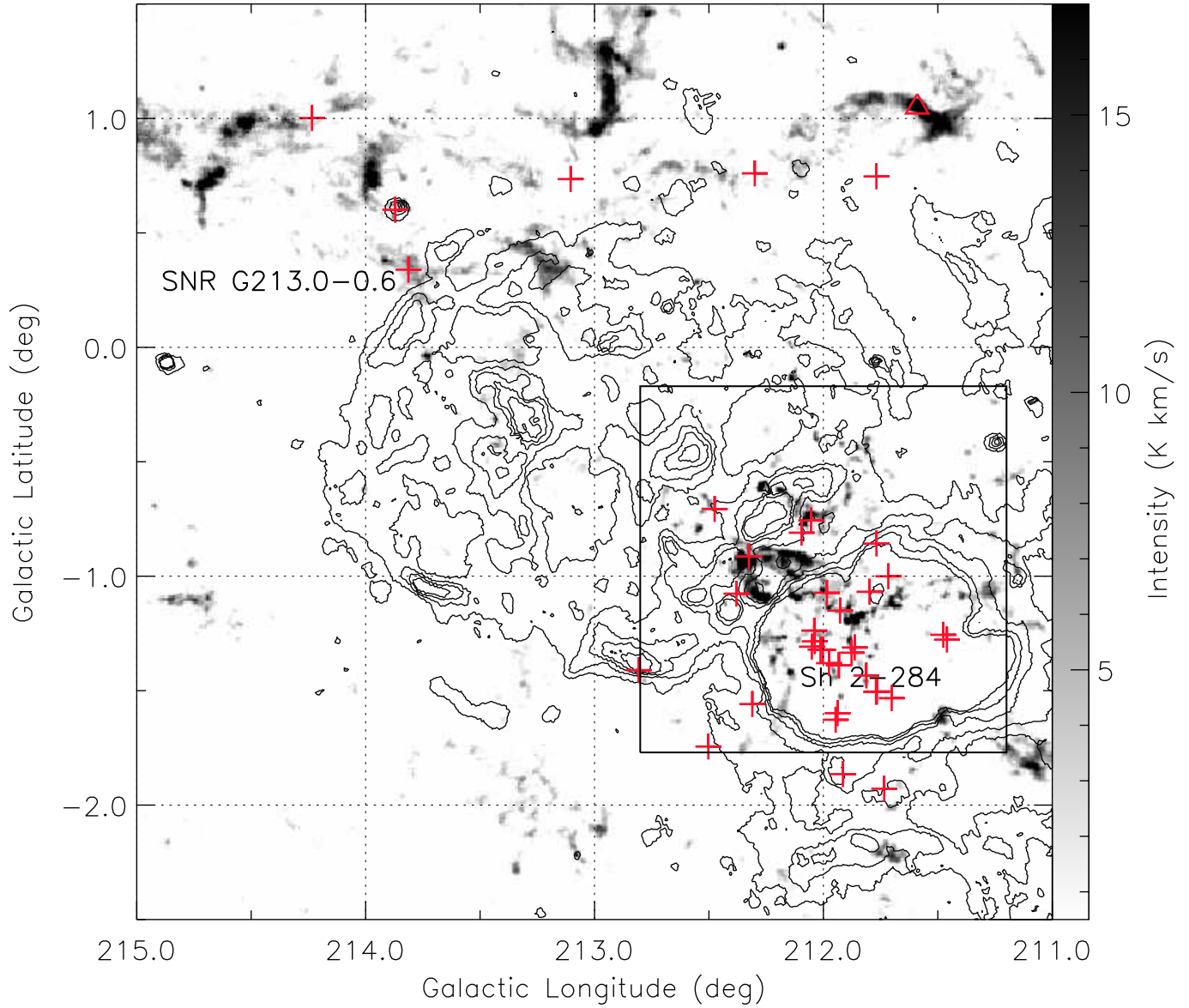


**Figure 19.** Integrated  $^{12}\text{CO}$  ( $J=1-0$ ) emission toward SNR G213.0–0.6 from 35 to 54  $\text{km s}^{-1}$ , overlaid with the same contours as in Figure 14. The red crosses indicate positions of early-type OB stars, which are probably associated with these MCs. The red triangle shows the maser source G211.59+01.05 at a parallax distance of 4.4 kpc (Reid et al. 2014). The lower-right box indicates the region shown in Figure 20.

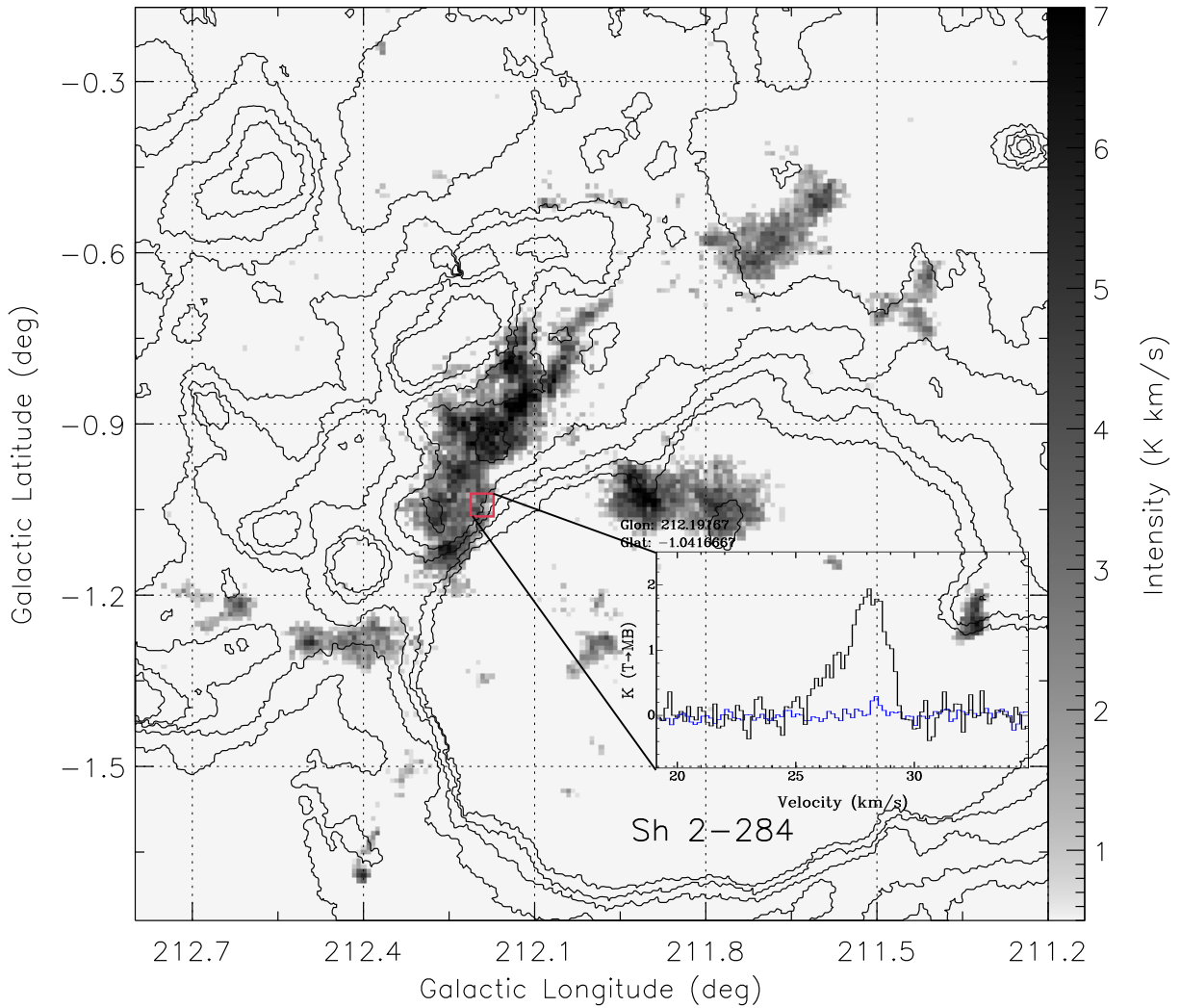


**Figure 20.** Integrated  $^{12}\text{CO}$  ( $J=1-0$ ) emission toward the southwestern boundary of SNR G213.0–0.6 from 24 to 33  $\text{km s}^{-1}$ , overlaid with the same contours as in Figure 14. The spectra of position  $l = 212^\circ.192$  and  $b = -1^\circ.042$  are also given ( $^{12}\text{CO}$  in black and  $^{13}\text{CO}$  in blue).